Analysis of Unforced Symmetric Instability in Mesoscale Eddies Using In Situ Observations

YAN BARABINOT,[a] CHRISTIAN BUCKINGHAM,[b] SABRINA SPEICH,[a] AND XAVIER CARTON[c]

[a] *Ecole Normale Supérieure, Laboratoire de Météorologie Dynamique, Paris Science Lettre University, Paris, France*
[b] *National Oceanography Centre, Southampton, United Kingdom*
[c] *Laboratoire d'Océanographie Physique et Spatiale, IUEM, Université de Bretagne Occidentale, Plouzané, France*

(Manuscript received 9 December 2024, in final form 5 September 2025, accepted 14 October 2025)

ABSTRACT: Symmetric instability (SI) is known to be effective in extracting kinetic energy from currents in frontal regions. This energy cascade involving SI has previously been observed at fronts at the sea surface, with wind forcing as the chief catalyst for destabilization. In this article, using in situ observations collected during the Elucidating the Role of Clouds–Circulation Coupling in Climate-Ocean–Atmosphere (EUREC4A-OA) cruise, we argue that North Brazil Current (NBC) rings could have been subject to symmetric instabilities using classical mathematical criteria even if they lie below the pycnocline. In particular, we demonstrate that the boundaries of mesoscale eddies could be the loci of unforced centrifugal–symmetric instabilities (CSIs) depending on the slope of isopycnal surfaces or, equivalently, the relative magnitudes of vertical and lateral stratifications. Assuming a gradient wind balance, this ratio implicitly accounts for curvature. We additionally analyze their primary sources of kinetic energy, accounting for the curvature. This analysis suggests that horizontal shear is likely the main driver of the disturbance's development. Finally, we estimate the characteristic time scale for the development of CSI and find that unforced symmetric modes may emerge within less than 1.5 days. Together, our results suggest that mesoscale eddies in the NBC may be intrinsically subject to symmetric instabilities owing to the centrifugal force, with potential implications for the life cycle of mesoscale eddies and transport of active/passive tracers by these oceanic phenomena.

KEYWORDS: Eddies; Instability; Small scale processes; In situ oceanic observations

1. Introduction

Oceanic submesoscale dynamics, characterized by horizontal scales of 0.1–10 km and temporal scales of hours to days, have attracted considerable attention in recent years. While this dynamical regime generates instabilities not present within the classical geostrophic or quasigeostrophic regime, several studies have nonetheless demonstrated its potential impact on global ocean dynamics (McWilliams 2016; Lévy et al. 2018; Buckingham et al. 2019; Naveira Garabato et al. 2019; Dong et al. 2021). Submesoscale currents and their associated instabilities are indeed believed to be one of the major pathways for energy loss of the large-scale ocean circulation, ultimately being dissipated at even finer spatial and temporal scales (Müller et al. 2005).

Among the types of instabilities that emerge in the ocean at these scales, centrifugal–symmetric instabilities (CSIs) are particularly effective at generating such a forward cascade (Thomas and Taylor 2010; D'Asaro et al. 2011; Gula et al. 2016b). In this article, we classify CSIs as the family of instabilities which occur when the Ertel potential vorticity multiplied by the Coriolis parameter is negative. To determine the type of CSI occurring (which includes inertial instability, mixed inertial/symmetric instability, purely symmetric instability, and gravitational/convective instability), we examine the instability's primary energy source. This is often called the energetic definition of CSI (Thomas et al. 2013). CSI is a form of inertial instability found within baroclinic fronts in which energy is chiefly extracted from the vertical shear in the front. Within such a front, the flow can be unstable to small disturbances in a direction inclined to the horizontal while remaining stable both inertially (i.e., absolute vorticity is positive) and gravitationally (i.e., stratification is positive). In its purest form, this instability induces an overturning cell with parcel motion principally along isopycnals but that may additionally contribute to the mixing of water masses (Buckingham et al. 2019; Naveira Garabato et al. 2019; Chor et al. 2022). This is why the instability is sometimes referred to as slantwise convection.

Historically, the study of CSI has been motivated by a desire to better understand the dynamics of atmospheric vortices (Rayleigh 1917; Solberg 1936; Fjortoft 1950; Ooyama 1966; Cho et al. 1993; Bowman and Shepherd 1995), and we refer the reader to Eliassen and Kleinschmidt (1957), van Mieghem (1951), Kloosterziel et al. (2007), and Kloosterziel (2010) for further details on the history of this phenomenon. In the ocean, CSI is believed to be active both near the surface (Taylor and Ferrari 2010; Thomas and Taylor 2010; D'Asaro et al. 2011; Thomas et al. 2013; Brannigan 2016; Gula et al. 2016a; Savelyev et al. 2018), in the bottom boundary layer, and topographic wakes (Allen and Newberger 1998; Gula et al. 2016b; Dewar et al. 2015; Wenegrat et al. 2018; Wenegrat and Thomas 2020; Molemaker et al. 2015; Naveira Garabato et al. 2019)—that is, in regions where stratification in density is reduced. Nonconservative processes such as friction and diabatic processes mostly occur at these ocean

---

Denotes content that is immediately available upon publication as open access.

Corresponding author: Yan Barabinot, yan.barabinot@lmd.ipsl.fr

DOI: 10.1175/JPO-D-24-0241.1

boundaries and are essential for driving the instability; for instance, potential vorticity (PV) is found to be modified near the ocean surface (Marshall et al. 1999, 2012), reducing stratification and triggering CSI development.

Relevant to the present study, frontal regions associated with oceanic mesoscale eddies have been identified as symmetrically unstable especially close to the ocean surface due to Ekman effects of wind (Brannigan et al. 2017). Wind forcing is indeed one of the major drivers of CSI in frontal regions (Thomas et al. 2013, 2016; Gula et al. 2016a; Buckingham et al. 2019; Yu et al. 2019). One therefore expects CSI to perturb the life cycle of mesoscale eddies by transferring their eddy kinetic energy to smaller scales as they do in other frontal regions. This phenomenon, in combination with gravitational instability, can also lead to the intense mixing of water masses and nutrients at the edge of eddies, impacting the transport of tracers by these structures (Brannigan 2016; Brannigan et al. 2017; Chor et al. 2022).

Boundaries of mesoscale eddies and the frontal region are places where we observe strongly slanted isopycnals and an associated geostrophic circulation (de Marez et al. 2020; Barabinot et al. 2024). One can therefore postulate that an eddy might be intrinsically symmetrically unstable without the influence of the wind. For example, CSI could potentially occur at the edge of mesoscale eddies where the slope of isopycnals is important, such as is the case for eddies perturbed by an intense background shear (Legras and Dritschel 1993; Mariotti et al. 1994). Recently, idealized three-dimensional numerical models showed that anticyclonic barotropic eddies can be spun off as the western boundary current crosses the equator. Symmetric instability then sets their PV to zero without taking into account the influence of the wind (Goldsworth et al. 2021). In this case, symmetric instability is triggered when Southern Hemisphere waters (with negative potential vorticity) are advected across the equator into the Northern Hemisphere. Symmetric instability thus becomes significantly strong. However, to the best of our knowledge, unforced symmetric instabilities have not yet been highlighted in eddies using in situ data, although some subsurface evidences of symmetric instability have already been found in the northwestern equatorial Pacific (Zhou et al. 2022).

In this article, using in situ data collected during the Elucidating the Role of Clouds–Circulation Coupling in Climate: Ocean–Atmosphere (EUREC4A-OA) experiment, we will show that North Brazil Current (NBC) rings can be subject to CSI using classical mathematical criteria derived from linear theory even if these eddies lie below the pycnocline. Their primary source of kinetic energy will be also analyzed using the approach of Thomas et al. (2013) and Chor et al. (2022). After revisiting the criteria for symmetric instability and applying these to in situ data, an analytical expression will be introduced to model the structure of sampled eddies and support the appearance of CSI in the observations. This will indicate that the signals of instability seen in the observations are not artifacts related to the design of the observational campaign. The article is organized as follows. In section 2, mathematical criteria for CSI are introduced. In section 3, the data and methods are described. In section 4, results obtained on in situ data are analyzed. In section 5, we present the analytical model and compare it to data. In section 6, we estimate the growth rate and corresponding time scales of CSI.

2. Theoretical aspects on CSI

a. Geostrophic flows

CSIs are defined as those that emerge, here in a geostrophic flow, when the Ertel PV q, multiplied by the Coriolis parameter f, is negative (Hoskins 1974; Haine and Marshall 1998):

$$fq < 0. \tag{1}$$

Hereafter, we refer to this criterion as Hoskins' criterion. Here, $q = (2\mathbf{\Omega} + \nabla \times \mathbf{v}) \cdot \nabla b \approx (f\mathbf{k} + \nabla \times \mathbf{v}_g) \cdot \nabla b$ with $\mathbf{k}$ being the local unit vector in the vertical, $\mathbf{v}_g$ being the horizontal geostrophic velocity, and $b = -g\rho/\rho_0$ (where g is the gravity, ρ is the density, and ρ_0 is a reference density) being the buoyancy. The quantity fq is the discriminant of the Hoskins–Ooyama equation [third unlabeled equation, Hoskins (1974)] which describes the evolution of across-stream perturbations to an inviscid, stably stratified parallel shear flow in geostrophic balance. The sign of the discriminant determines the nature of the equation (i.e., whether it is elliptic or hyperbolic). For positively stratified geostrophic flow away from the equator, the discriminant can be rewritten in a convenient nondimensional form:

$$q^* = 1 + \mathrm{Ro}_d - \mathrm{Ri}_d^{-1} < 0, \tag{2}$$

where $\mathrm{Ro}_d = \zeta_g/f$ and $\mathrm{Ri}_d = N^2/|\partial_z \mathbf{v}_g|^2 = f^2N^2/|\partial_r b|^2$ are the dynamical Rossby and Richardson numbers, respectively. In these expressions, $\partial_r b$ refers to the radial gradient of buoyancy, $\partial_z \mathbf{v}_g$ refers to the vertical shear, and ζ_g refers to the vertical geostrophic relative vorticity (i.e., the vertical component of the vorticity vector). From this second equation, we observe that order-one Richardson numbers and order-one Rossby numbers represent favorable conditions for overturning instabilities, which occur when $fq < 0$.

Equation (1) can be satisfied for several instabilities, including gravitational ($N^2 < 0$), inertial ($\zeta_g/f < -1$), and symmetric instabilities ($fq < 0$ but when $N^2 > 0$ and $\zeta_g/f > -1$). To discriminate between these instabilities, Thomas et al. (2013) introduced the following angles (hereafter Thomas' instability angles):

$$\phi = \arctan(-\mathrm{Ri}_d^{-1}), \tag{3a}$$

and the critical angle:

$$\phi_c = \arctan[-(1 + \mathrm{Ro}_d)]. \tag{3b}$$

These angles summarize the contributions of barotropic and baroclinic shear to the onset of the instability (Thomas et al. 2013; Hamlington et al. 2014), mapping dynamically relevant values in (Ro_d, Ri_d) space to visually informative values in (ϕ, ϕ_c) space. Expressed in units of degrees, $\phi > \phi_c$ refers to the stable state, $-45° < \phi < \phi_c$ refers to the case where mixed inertial/symmetric instability can develop, $-90° < \phi < -45°$

refers to the case where purely symmetric instability can develop, $-135° < \phi < -90°$ refers to the case where the flow is symmetrically and gravitationally unstable, and $-180° < \phi < -135°$ refers to the case where the flow is gravitationally unstable. Note, these criteria are valid for anticyclonic flow ($\mathrm{Ro}_d < 0$). For the case of cyclonic flow ($\mathrm{Ro}_d > 0$), the only difference is that inertial instability is mathematically not possible (Carton 2001). In the following, Thomas' instability angles will be used as an additional check on the type of instability occurring. Thomas' angles will predict instability if and only if $fq < 0$. This is not an additional criterion.

b. *Cyclogeostrophic flows*

Equation (1) and subsequent relations do not take into account centrifugal forces experienced by fluid parcels, for example, within a cyclogeostrophic flow, and therefore are not necessarily valid in the study of eddies. To better approximate the dynamics in such cases, Buckingham et al. (2021a,b) proposed the use of a baroclinic form of the generalized Rayleigh criterion, $Lq < 0$, or

$$L^{*}fq = (1 + \mathrm{Cu})fq < 0, \tag{4}$$

where $L = rv_\theta + (1/2)fr^2$ is the vertical component of absolute angular momentum, $L^* = 1 + \mathrm{Cu}$ is a nondimensional form of this quantity, r is a radius or radius of curvature whose origin is the vortex center, and v_θ denotes the azimuthal or alongfront velocity of a curved front. Note that the right term in Eq. (4) has the same units as in Eq. (1) but introduces a local, signed, nondimensional number, $\mathrm{Cu} = 2v_\theta/(rf)$, quantifying the curvature of the flow; it tends to be positive for cyclonic flow and negative for anticyclonic flow. This number follows naturally from the expression describing gradient wind balance, $f(1 + \mathrm{Cu})\partial_z \mathbf{v} = \partial_r b$, where Cu is seen as a deviation in the thermal wind balance. Alternatively, Cu can be interpreted as a Rossby number based on the curvature vorticity $2v_\theta/r$ (F. Goldsworth 2023, personal communication). Last, as mentioned, Cu is a locally valid, nondimensional form of L. Interestingly, while L is conserved on the sphere at small horizontal scales (unpublished proof), owing to the WKB approximation made during its derivation, the criterion [cf. Eq. (4)] remains applicable across latitudes so long as a locally valid f is used. Examining L^*fq and comparing with fq are therefore a helpful analysis.

The corresponding nondimensional form of Eq. (4) is obtained by assuming positive stratification away from the equator and nonzero r:

$$L^{*}q^{*} = (1 + \mathrm{Cu})(1 + \mathrm{Ro}_d) - (1 + \mathrm{Cu})^2\mathrm{Ri}_d^{-1} < 0. \tag{5}$$

This quantity L^*q^* is useful for estimating growth rates of the instability (Buckingham et al. 2021a). This is done in section 6. In this expression, Ro_d and Ri_d are computed, assuming a gradient wind balance as detailed in Buckingham et al. (2021a).

While Eq. (4) provides a criterion that is valid not only just for parallel shear flow but also for flows with curvature, it should be noted that the sign of fq often yields a qualitatively correct solution and is helpful for detecting the kinds of instabilities that might occur. In the work that follows, we therefore apply the two criteria: Eq. (1) for Hoskins' geostrophic criterion with Eq. (3) for Thomas' angles and Eq. (4) for the cyclogeostrophic criterion of Buckingham et al. (2021a,b). Additionally, we use Eq. (5) to estimate time scales for the growth of CSI (section 6).

ENERGETICS

Assuming linear theory, we can characterize the primary energy sources for the disturbance at the onset of CSI (Thomas et al. 2013; Chor et al. 2022). For the purposes of this paper, we focus on the rates of horizontal shear production (HSP, associated with the inertial/centrifugal modes) and vertical shear production (VSP, associated with symmetric modes). Recall, the energy source for CSI differs depending on the relative magnitudes of barotropic and baroclinic components of the discriminant (i.e., fq or L^*fq). Hence, while ϕ_c and ϕ can be used to discern the primary energy source of CSIs within a geostrophic flow, these expressions must be altered to reflect the curvature of the flow or, equivalently, impact of the centrifugal force. Hence, in appendix A, we revisit the turbulent kinetic energy (TKE) budget and account for this deviation from geostrophy. Briefly, assuming a background flow under gradient wind balance with parcel motion predominantly along isopycnals, we find that under linear theory the ratio of horizontal to vertical shear production is

$$R_{\mathrm{SP}} = \mathrm{HSP/VSP} = -\frac{\mathrm{Ro}_d\,\mathrm{Ri}_d}{(1 + \mathrm{Cu})}\left(1 - \frac{\mathrm{Cu}}{\mathrm{Ro}_d}\right). \tag{6}$$

Here, the ratio is cast in a form comparable to that presented by Chor et al. (2022). When the curvature is zero, we retrieve $R_{\mathrm{SP}} = -\mathrm{Ro}_d\mathrm{Ri}_d$, which is equivalent to the geostrophic expressions used by Chor et al. (2022) and Kimura (2024)–i.e., their Eqs. (4) and (29), respectively.

3. Data and methods

a. *EUREC4A-OA in situ data*

The EUREC4A-OA campaign took place between 20 January and 20 February 2020 (Stevens et al. 2021; Speich and The Embarked Science Team 2021). We focus here on two anticyclonic eddies sampled along the continental slope of Guyane by the French Research Vessel (R/V) *L'Atalante*. One of the anticyclonic eddies is a surface-intensified eddy and has been identified as an NBC ring (Subirade et al. 2023). Its velocity structure extends to a depth of 150 m. The other is a subsurface-intensified anticyclone (with more of an intrathermocline structure). Its core is located between 200- and 600-m depth and lies just below the surface NBC ring. [Note: This vertical superposition of anticyclonic eddies in the NBC is not new but has previously been studied (e.g., Napolitano et al. 2024).] The subsurface eddy has been sampled by two vertical sections. Hydrographic observations were made using research vessel–based conductivity–temperature–depth (CTD), underway CTD (uCTD), and lowered acoustic Doppler current profiler (L-ADCP) measurements. A moving vessel profiler (MVP) was also used to observe the surface-intensified eddy but resulted in only a few vertical profiles on the eastern side of the eddy (Speich and The Embarked Science Team 2021; L'Hégaret et al. 2023). A total of 25 and 24 CTD/uCTD

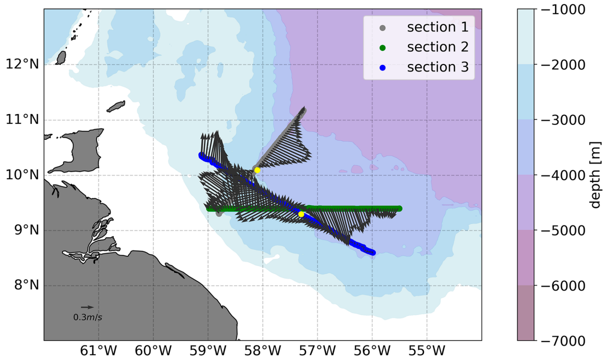

FIG. 1. Velocity vector field at $z = -250$ m for the subsurface AE sampled by sections 1 (gray) and 3 (blue) and $z = -50$ m for the surface AE of EUREC4A-OA (green). The regional bathymetry from the ETOPO2 dataset (Smith and Sandwell 1997) is shown in the background as colored shading, as is the estimated center (the yellow square) of the eddy computed from the observed velocities using the Nencioli et al. (2008) method. The center is defined as the point where the mean radial velocity is minimum.

profiles sampled the NBC ring and the subsurface eddy, respectively. A total of 17 CTD/uCTD profiles sampled the subsurface eddy for the second section. The eddy velocity field was also measured by two ship-mounted ADCPs (S-ADCPs) with sampling frequencies of 38 and 75 kHz. Temperature and salinity were measured by the CTD with an accuracy of ±0.002°C and ±0.005 psu, respectively. The temperature and salinity accuracies of the uCTD are ±0.01°C and ±0.02 psu, respectively, while horizontal velocities from the S-ADCP have accuracies of approximately ±3 cm s^{-1}. See L'Hégaret et al. (2023) for more information on the in situ data collected during the EUREC4A-OA fieldwork.

The in situ measurements were made along sections defined in Fig. 1, where the distance between stations is not uniform. We define the resolution of each section as the average of all distances between its successive soundings.

Given the shorter time scales associated to CSI features, we provide the time periods, and the observations used in the individual sections were taken over [see the cruise report from Speich and The Embarked Science Team (2021)]. Table 1 gathers information about resolutions and time periods.

For the purpose of this study, it is important that the in situ section of the eddies crosses the eddy centers to reduce errors made by not considering the real eddy center. In Fig. 1, using the S-ADCP data and the eddy center detection method of Nencioli et al. (2008), we show that this was the case for the data examined here. Briefly, the Nencioli et al. (2008) routine builds a two-dimensional grid around the section at a given depth level. Then, it estimates the eddy center by minimizing the mean radial velocity.

b. *Data processing and computations*

Raw data were calibrated, quality controlled, and subsequently interpolated to an evenly spaced grid (L'Hégaret et al. 2023). To limit spurious effects, we performed linear interpolations only in **x** (here radial) and **z** (vertical) directions. The data were then smoothed with a numerical fourth-order, low-pass filter (scipy.signal.filtfilt in Python) to avoid overshoots when computing gradients. The choice of thresholds (or cutoff length associated with the cutoff wavenumber) is subjective and depends on the scales studied. As we were considering mesoscale eddies, we choose thresholds $L_x = 20$ km and $L_z = 20$ m for the horizontal and vertical length scales. The cutoff length associated with (L_x, L_z) of filters is chosen to be longer than the spatial sampling of the calibrated data. Nevertheless, this mapping could lead to artifacts when computing gradients, and we perform a sensitivity study in appendix B. Results show that even when choosing higher values for (L_x, L_z), fields remain unchanged at the mesoscale, especially for instability criteria.

Filtering is also necessary to damp the influence of inertia–gravity waves (IGWs). With $L_x = 20$ km, IGWs with wavenumbers higher than $2\pi/L_x = 3.1 \times 10^{-4}$ m^{-1} are reduced. According to the sensitivity study, a value of $L_x = 50$ km does not change fields. Therefore, IGWs with wavenumbers higher than 1.3×10^{-4} m^{-1} do not impact our results. On the f plane, the IGW dispersion relation is given by $\Omega^2 = f^2 + N^2 k_H^2/k_\perp^2$, where Ω is the wave frequency, N^2 is the stratification, and $(k_H, k_\perp)$ is the horizontal and vertical wavenumbers. Noting the horizontal and vertical length scales as L_x and H, we can find scales for the wave's time period. According to the dispersion relation with $L_x > 50$ km and $H = 500$ m (approximately the vortex height), IGWs with smaller wavenumbers than 1.3×10^{-4} m^{-1} have a period larger than 43 h. This is approximately the time needed to conduct cross sections of the eddies so our data may contain residual signals from these waves. However, as we will see, instability criteria are satisfied in thin regions of width smaller than 50 km. We can thus remain confident in our results.

To apply formulas (1), (3), and (4) to two-dimensional in situ vertical sections, we first decomposed the measured velocities into a transverse component $v_\perp$ and a longitudinal component $v_\parallel$ with respect to the ship transect so that $v_\perp$ represents the orthoradial velocity in a cylindrical coordinate system for a perfect section passing through the center of a circular vortex. The appearing eddy center on a ship section is thus the location where $v_\perp$ is zero at each depth.

TABLE 1. Basic information on sections sampling eddies.

	uCTD/CTD resolution		ADCP resolution		Time periods		
Sections	Horizontal (km)	Vertical (m)	Horizontal (km)	Vertical (m)	Start	End	Total
1	8.4	1	<0.3	8	1100 UTC 11 Feb	0134 UTC 13 Feb	1 day 14 h 40 min
2	9.2	1	<0.3	8	0030 UTC 26 Jan	0200 UTC 29 Jan	2 day 13 h 30 min
3	11.3	1	<0.3	8	0800 UTC 8 Feb	1200 UTC 10 Feb	2 day 4 h

Therefore, the derivatives of a scalar quantity a were approximated by a second-order scheme as follows:

$$\partial_r a(r,z) \approx \frac{a(r+\Delta r, z) - a(r-\Delta r, z)}{2\Delta r}, \tag{7}$$

$$\partial_z a(r,z) \approx \frac{a(r, z+\Delta z) - a(x, z-\Delta z)}{2\Delta z}. \tag{8}$$

We then compute the geostrophic velocity v_g using the thermal wind balance (Laxenaire et al. 2019; de Marez et al. 2020). Thus, we write

$$v_g(r,z) = v_\perp(r, z_{\max}) - \int_{z_{\max}}^{z} \frac{\partial b}{\partial r}(r,z')dz', \tag{9}$$

where $z_{\max}$ is the deepest geopotential level of the sections, $\rho_0 = 1000\ \mathrm{kg\ m^{-3}}$, and $v_\perp(r, z_{\max})$ is the measured orthogonal velocity to the ship track at $z_{\max}$. As the velocity field rarely vanishes at the deepest geopotential level of the sections, this boundary condition ensures a more faithful velocity profile Johns et al. (1989).

To derive the geostrophic relative vorticity, we estimated $\zeta_g = \partial_r v_g + v_g/r$ at each depth. It appears that the term v_g/r diverges in the eddy core since v_g does not go to zero as fast as r, at the center. This divergence leads to uncertainties in applying the previous criteria. Accounting for the resolution and the ADCP uncertainty, the uncertainty on this term is $(v_g \pm \Delta v_g)/(r \pm \Delta r)$. Using a Taylor expansion, the relative error on v_g/r is simply $(\Delta v_g/v_g) + (\Delta r/r) + (\Delta v_g/v_g) \times (\Delta r/r)$. This quantity can be computed on each vertical section, and results are less reliable when this quantity is lower than 20%. The largest uncertainty is due to the term involving the horizontal resolution $(\Delta r/r)$; the threshold of 20% is reasonable as the eddy radii do not exceed 100 km with a horizontal resolution on the order of 10 km.

For a two-dimensional vertical section sampling an eddy, the geostrophic Ertel PV is thus approximated as

$$q = -\frac{1}{f}\left(\frac{\partial b}{\partial r}\right)^2 + \left(\frac{\partial v_g}{\partial r} + \frac{v_g}{r} + f\right)\frac{\partial b}{\partial z}. \tag{10}$$

In appendix C, we discuss this axisymmetry approximation. Note: No particular eddy dynamics are assumed. For example, we do not assume that the flow is in cyclogeostrophic balance; we simply neglect orthoradial variations, as well as the vertical velocity, arguing that these terms are small relative to other terms in the expression. In appendix D, we discuss the influence of data resolution on CSI criteria and results.

4. Results on in situ observations

To detect regions subject to CSI, we applied the two criteria [from one side the geostrophic criterion of Hoskins (1974) with Thomas' angles and from the other side the cyclogeostrophic criterion of Buckingham et al. (2021a,b)] to the three sections sampling NBC rings. Results are presented in Fig. 2.

In the first section (which sampled the subsurface structure in its center), both anticyclonic eddies are visible: the surface one above −100 m and the subsurface below the pycnocline. Regions where Hoskins' ($fq < 0$) and Buckingham's ($L^*fq < 0$) criteria are visible in blue are outside the hatched regions especially around $x = 100$ km for the surface ring and around $x = 160$ km for the subsurface eddy in Figs. 2a,d and g. According to Thomas' angles, the boundary is more subject to inertial/symmetric instability than to purely symmetric instability. As might be expected, the criterion of Buckingham et al. (2021a,b) does not provide the same result as the Hoskins' criterion. Some layering is noticeable around −200 m at the top of the subsurface eddy by the yellow spot. This layering has been identified as staircase layering by Barabinot et al. (2024).

In the second section which sampled the surface structure in its center, both anticyclonic eddies are also visible: the surface one above −150 m and the subsurface below the pycnocline. On the boundary of eddies, blue regions representing regions where criteria for CSI are met can be found. Blue regions are also found close to the surface around −30 m in the structure of the surface NBC ring, maybe due to the wind forcing.

In the third section, the geostrophic and cyclogeostrophic criteria only reveal layered regions at the top of the subsurface anticyclonic eddy. This section has sampled the subsurface anticyclonic eddy quite far from its center, and the appearing vertical shear is thus lower than in section 1. For the three sections, regions where Buckingham's criterion is matched are characterized by $1 + \mathrm{Cu} < 0.2$ (not shown).

Overall, based on the three criteria, CSI can develop in regions where the horizontal buoyancy gradient is maximal, that is, the inflection points of isopycnals. Figure 3 presents their primary source of kinetic energy when curvature is taken into account or not. In the case $\mathrm{Cu} = 0$, eddy cores, defined as regions inside the maximum velocity contour, are characterized by regions where the horizontal shear production is larger than the vertical shear production. Regions subject to CSI in eddy cores are thus more driven by the horizontal shear. This is the case for both surface and subsurface eddies where regions characterized by Buckingham's criterion are mostly included in regions where the horizontal shear production exceeds the vertical shear production ($R_{\mathrm{SP}} > 1$).

On the contrary, boundaries are characterized by a ratio lower than unity showing that the vertical shear drives more CSI development. In the case of the subsurface anticyclonic eddy, it is thus interesting to note that CSIs are more driven by the horizontal shear for lateral boundaries but by the vertical shear for top and bottom boundaries (especially looking at regions close to isopycnals 26.5 and 27 kg m^{-3}). For the surface structure, we also recover the same tendency with red spots ($L^*fq < 0$) not only included in regions where the horizontal shear production exceeds the vertical shear production ($R_{\mathrm{SP}} > 2$) on the lateral boundaries (at $x = 70$ and 250 km, $z = -50$ m) but also included in regions where the vertical shear production exceeds the horizontal shear production ($R_{\mathrm{SP}} < 1$) on the bottom boundary especially close to isopycnal 24.5 kg m^{-3}.

When considering the local curvature of the flow $\mathrm{Cu} \neq 0$, the entire subsurface structure (Fig. 3d) appears white (i.e., $R_{\mathrm{SP}} > 2$), revealing that CSI is more driven by the horizontal shear. In the second section (Fig. 3b), regions where the vertical shear production exceeds the horizontal shear production

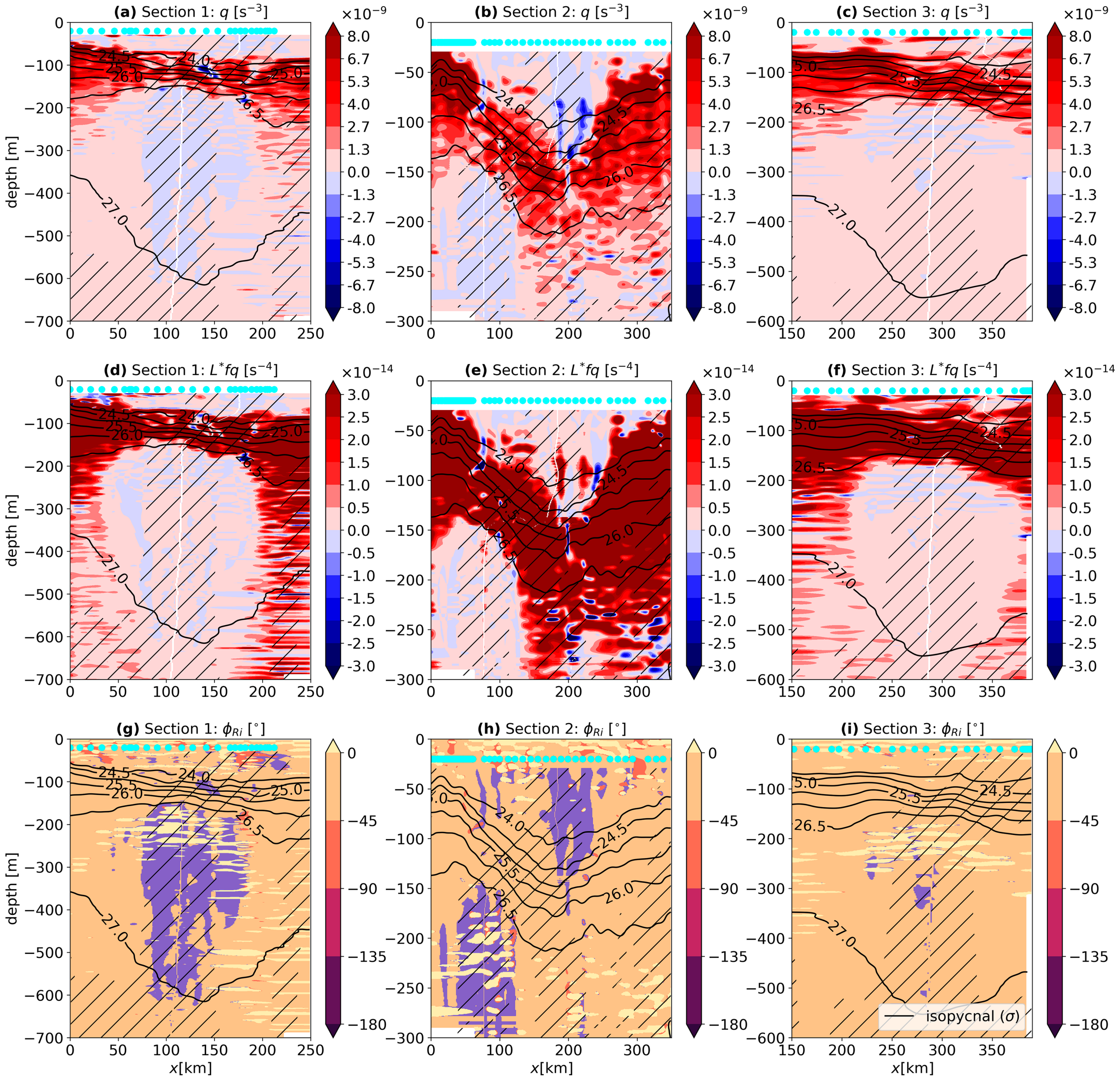

FIG. 2. Necessary conditions for CSI applied on vertical sections. The (a)–(c) q, (d)–(f) L^*fq, and (g)–(i) ϕ. (a),(d),(g) Section 1, (b),(e),(h) section 2, and (c),(f),(i) section 3. For (a)–(f), negative values are met in blue regions. For (g)–(i), blue patches indicate regions where $-45° < \phi < \phi_c$. The hatches represents regions where criteria cannot be trusted. Cyan dots indicate the location of the uCTD/CTD profiles. Dark lines represents isopycnal surfaces, and in (a)–(f), the white line indicates the eddy center.

($R_{\rm SP} < 1$) are mostly located at the interface between the two anticyclonic eddies. Accounting for the local curvature of the flow does not change the primary sources of CSI for the surface structure. However, via the subsurface case, we show that curvature has significant implications for CSI development notably on the primary source of kinetic energy.

5. Analytical prediction for CSI in mesoscale eddies

To apply CSI criteria to two-dimensional vertical sections, we interpolated and smoothed the data to avoid overshoots when computing gradients. This methodology can lead us to identify instability where there is none. To show that the signals of instability seen in the observations are not artifacts related to the design of the observational campaign, our objective is now to model analytically the mesoscale structure of eddies to apply CSI mathematical criteria. As the eddy of section 1 is not connected to the ocean surface, this model will demonstrate that such an eddy is subject to CSI just because of its mesoscale density and velocity gradients. We explore the use of an analytical model to reproduce the eddy structure observed in sections 1 and 2.

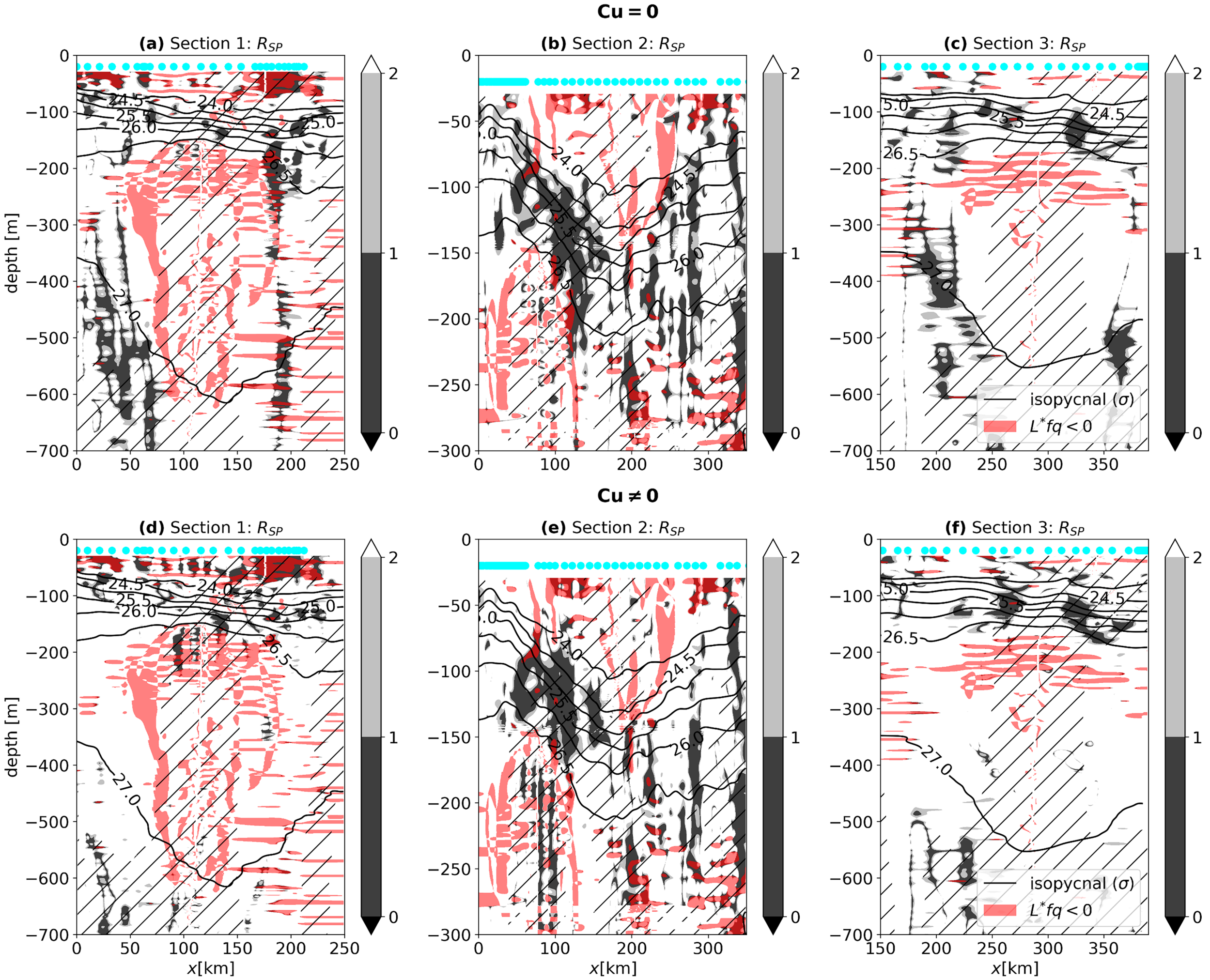

FIG. 3. Sources of kinetic energy for the disturbances in each section. Shaded colors denote R_{SP} = HSP/VSP as follows: $0 < R_{\mathrm{SP}} < 1$ (dark gray), $1 < R_{\mathrm{SP}} < 2$ (light gray), and unstable regions $L^*fq < 0$ (light red). (top) Results without curvature (Cu = 0) and (bottom) results when considering the curvature (Cu ≠ 0).

We assume that the sampled eddies are axisymmetric, although this is not exactly the case in Fig. 2 as we note several asymmetrical structures in these sections. We also approximate the eddy core or center as perfectly vertical and neglect outcropping of isopycnals. In a cylindrical frame of reference, noting σ as the total potential density and $\overline{\sigma}$ as the average potential density representing an ocean at rest, an eddy is associated with a density anomaly σ' such that $\sigma'(r, z) = \sigma(r, z) - \overline{\sigma}(z)$. In this approach, we do not construct an analytical model of the stratification profile. Instead, we use a climatological average building with Argo floats (Laxenaire et al. 2019; Barabinot et al. 2024). After determining the eddy center using the routine of Nencioli et al. (2008), a square with side 0.5° is constructed around the estimated center so that it lies at the intersection of the diagonals. Then, using the Coriolis database (https://www.coriolis.eu.org/), all temperature, salinity, and potential density profiles sampled by Argo profiling floats over 20 years in this area are assembled, and their values are averaged over the geopotential levels.

According to Bretherton (1966), the anomaly of density is linked to the stratification and to isopycnals deviation η with the relation

$$\sigma'(r, z) = -\eta(r, z)\frac{d\overline{\sigma}}{dz}. \tag{11}$$

According to studies based on experiments, vortices in stratified media with a constant stratification reflect a Gaussian shape in the vertical (Aubert et al. 2012; Flór 1994; Beckers et al. 2001; Bonnier et al. 2000; Negretti and Billant 2013; Mahdinia et al. 2017). In the horizontal plane, Carton and McWilliams (1989) proposed an exponential alpha profile. Therefore, Barabinot et al. (2025) proposed to model $\eta(r, z) = \eta_z(z)\chi(r)$ as follows:

$$\chi(r) = \exp\left[-\left(\frac{r}{R}\right)^{\alpha}\right], \tag{12}$$

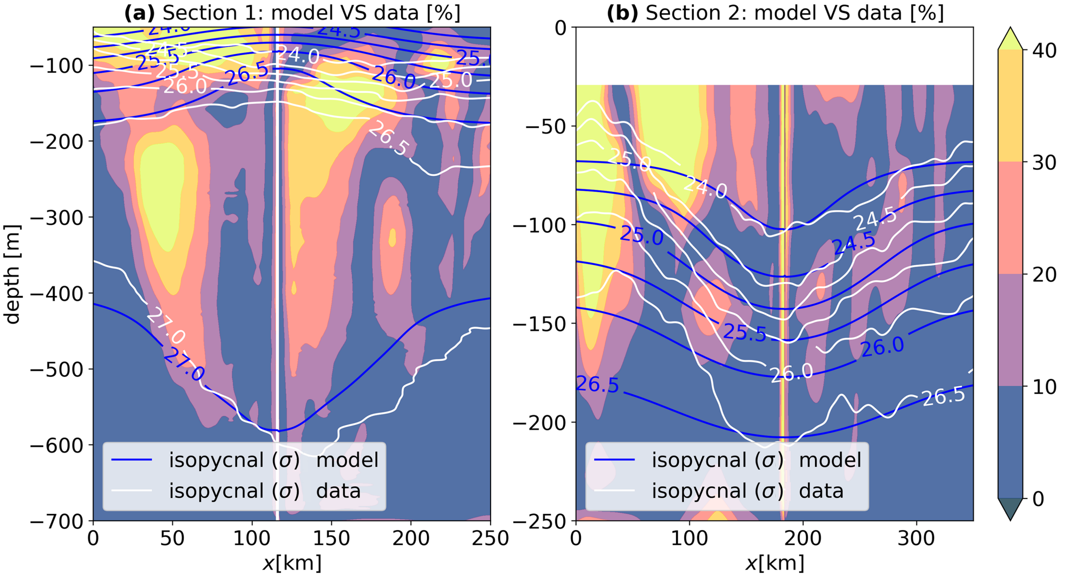

FIG. 4. Relative error between the model and the data for the velocity in (a) section 1 and (b) section 2. The color bar represents the relative error values as a percentage. For each panel, we depict observed isopycnals (white contours) and modeled isopycnals (blue contours).

$$\eta_z(z) = \eta_0\left(\frac{z - z_1}{H}\right)\exp\left[-\left(\frac{z - z_1}{H}\right)^2\right] + \eta_1, \qquad (13)$$

where η_0 is the amplitude of isopycnal deviation, R is the eddy radius, z_1 is the location of the median plane (where the anomaly cancels), H_1 is the characteristic vertical height of the eddy, and η_1 is a potential offset that we find in data. We thus fit this formula to sections 1 and 2 to model the eddy structure, respectively, of the subsurface and surface anticyclonic eddies. A nonlinear least square algorithm is used to find optimized parameters. For the subsurface eddy of section one, we found $\eta_0 = 276$ m, $R = 88$ km, $z_1 = -343$ m, $H_1 = 385$ m, $\eta_1 = -72$ m, and $\alpha = 2$. For the surface NBC ring, we found $\eta_0 = 146$ m, $R = 94$ km, $z_1 = -55$ m, $H_1 = 139$ m, $\eta_1 = 2$ m, and $\alpha = 2$. Note that the formula for χ has already been tested on NBC rings and is a reasonably good approximation of the velocity structure but tends to underestimate the maximum velocity and smooth the velocity profile (Castelão and Johns 2011). Therefore, velocity gradients might be reduced.

The NBC ring can have a Gaussian shape, which is a self-similar solution of the diffusion equation. The well-known Lamb–Oseen vortex for incompressible and unsteady flow is an example of such a solution (Oseen 1912). Here, both anticyclonic eddies can be modeled using $\alpha = 2$.

The nonconstant stratification influences the vertical shape of the density anomaly and breaks the eddy's vertical symmetry with respect to its median plane (which is defined by the location where isopycnals are horizontal) as we observe it in Figs. 2 and 3. Once the anomaly has been modeled, we compute the geostrophic velocity v_g as in Eq. (9):

$$v_g(r, z) = v_\perp(r, z_{\max}) - \frac{g}{\rho_0 f}\int_{z_{\max}}^{z}\frac{\partial\sigma'}{\partial r}(r, z')dz'. \qquad (14)$$

To compare the measured velocity with our model, we then chose to introduce an ageostrophic component to this velocity field using the cyclogeostrophic balance. However, the exact solution detailed in Douglass and Richman (2015) and Ioannou et al. (2017) appears to be problematic close to the eddy center as described in Penven et al. (2014) and Arnason et al. (1962). As a result, we compute an approximated cyclogeostrophic solution following Penven et al. (2014) such that

$$v_c(r, z) = v_g(r, z) - \frac{v_g^2(r, z)}{fr}. \qquad (15)$$

To evaluate the validity of our analytical model, the relative error defined by $|v_{\mathrm{mod}}(r, z) - v_{\mathrm{data}}(r, z)|/\max(|v_{\mathrm{data}}|)$ is calculated. Results are shown in Fig. 4. Overall, we note that isopycnal surfaces are in good agreement between the data and the model even if we cannot model the interaction between both eddies, in particular above −150-m depth in Fig. 4a and below −100 m in Fig. 4b. Locations where the relative error is higher than 20% correspond to the region of maximum velocity. It is important to note that velocities are smaller in the model than in the observations. Error could be caused by violation of the assumption of cyclogeostrophy in the eddy. It could also arise from the assumption of the functional form of the density structure or our assumed boundary conditions.

Results on CSI criteria can be found in Fig. 5 for, respectively, the subsurface and surface anticyclonic eddy of sections 1 and 2. Eddies reconstructions are not symmetric because the boundary condition of Eq. (9) is not symmetric.

Similarly to the observations, a clear negative region of fq and L^*fq can be found in the periphery of the subsurface structure and in the core of the surface NBC rings showing that theoretically both structures are subject to CSI according to Hoskins' and Buckingham's criteria. Thomas' angles also

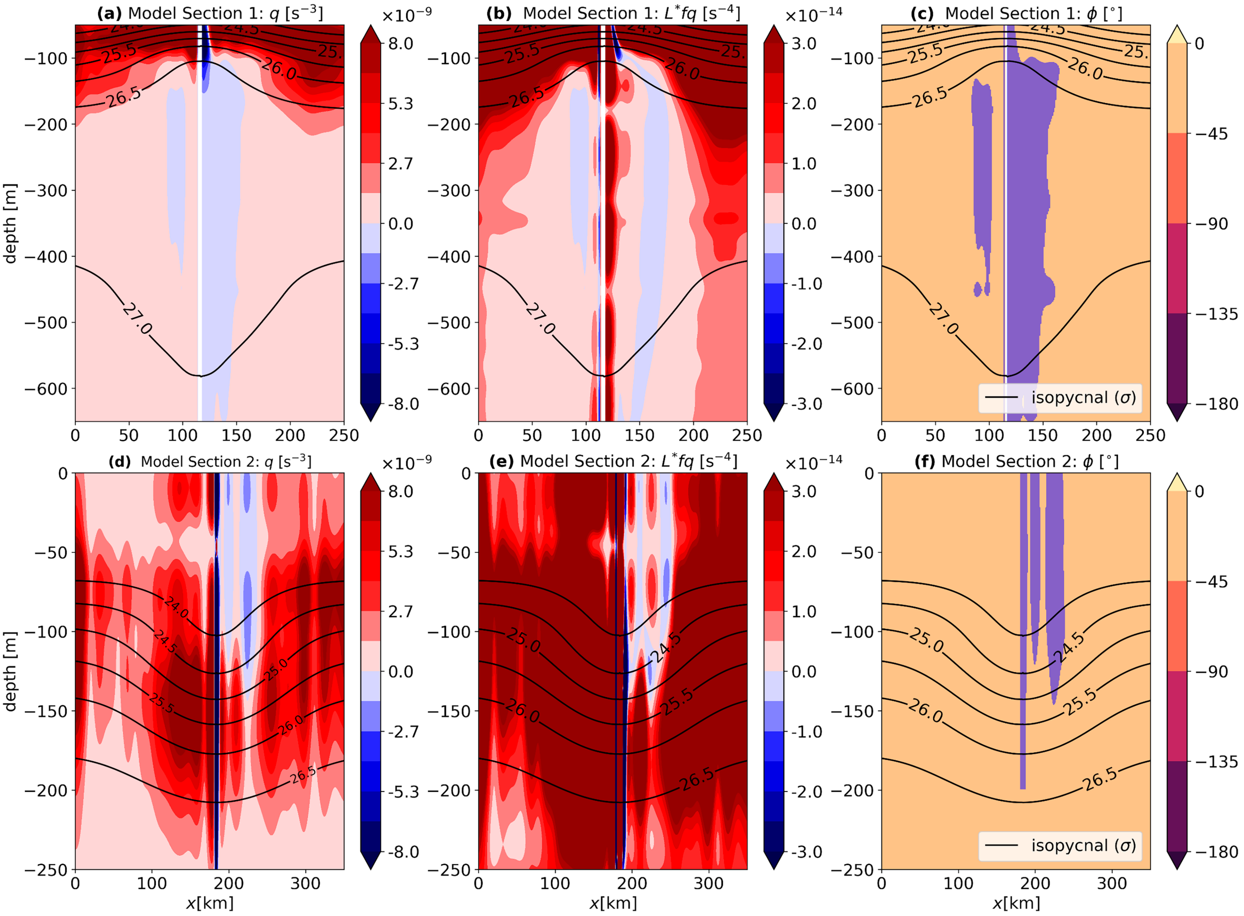

FIG. 5. Geostrophic (Hoskins 1974) and cyclogeostrophic criteria (Buckingham et al. 2021a,b), as well as instability angles (Thomas et al. 2013) for the analytical models of (top) section 1 and (bottom) section 2. Illustrated criteria include (a),(d) $q < 0$, (b),(e) $L^*fq < 0$, and (c),(f) Thomas' instability angle ϕ, with each column highlighting these different criteria. Again, solid black lines correspond to isopycnal surfaces.

show a region of CSI (blue region) with $L^*fq < 0$ and $\phi < \phi_c$, therefore showing that inertial/symmetric instability is likely. This region is less marked for the surface anticyclonic structure. Logically, blue regions close to the surface that can be observed in data do not appear in the model which does not include any outcropping nor wind influence. Overall, note that both the amplitude of criteria and regions subject to CSI are well predicted by the model.

In Fig. 6 is represented the ratio between the horizontal to vertical shear production of kinetic energy following Eq. (6) and using the analytical model. Both cases $\mathrm{Cu} = 0$ and $\mathrm{Cu} \neq 0$ are plotted. For the subsurface anticyclonic eddy, in both cases, the horizontal shear appears as the primary source of kinetic energy for the lateral eddy boundaries. However, the vertical shear is predominant at the top or at the bottom boundaries which is consistent with the azimuthal flow decreasing at the eddy top or bottom. On the contrary, for the surface anticyclonic eddy, the horizontal shear is the main driver of CSI development. It is worth noting that other phenomena such as wind forcing could impact the development of CSI (Thomas et al. 2013; Brannigan et al. 2017). In our study, the analysis is performed without explicitly considering the effects of frictional and buoyancy fluxes on CSI; however, because we are using a climatological average based on observations, the impact of surface forcing may be implicitly contained within the observed near-surface N^2, preconditioning the upper ocean to instances of CSI (Buckingham et al. 2016). It is highly unlikely such forcing would impact N^2 below the pycnocline.

6. Characteristic time scale for the growth of CSI

In this last section, using both data and the analytical model, the aim is to assess the order of magnitude for the linear growth rate of CSI. We focus on the subsurface anticyclonic eddy as, in that case, CSI cannot be influenced by any wind forcing. According to Eq. (A28) of Buckingham et al. (2021a) [see also Eq. (7) of Brannigan et al. (2017)], for modes aligned with isopycnals (i.e., $k/m = M^2/N^2$ with k and m being the radial and vertical wavenumbers of the

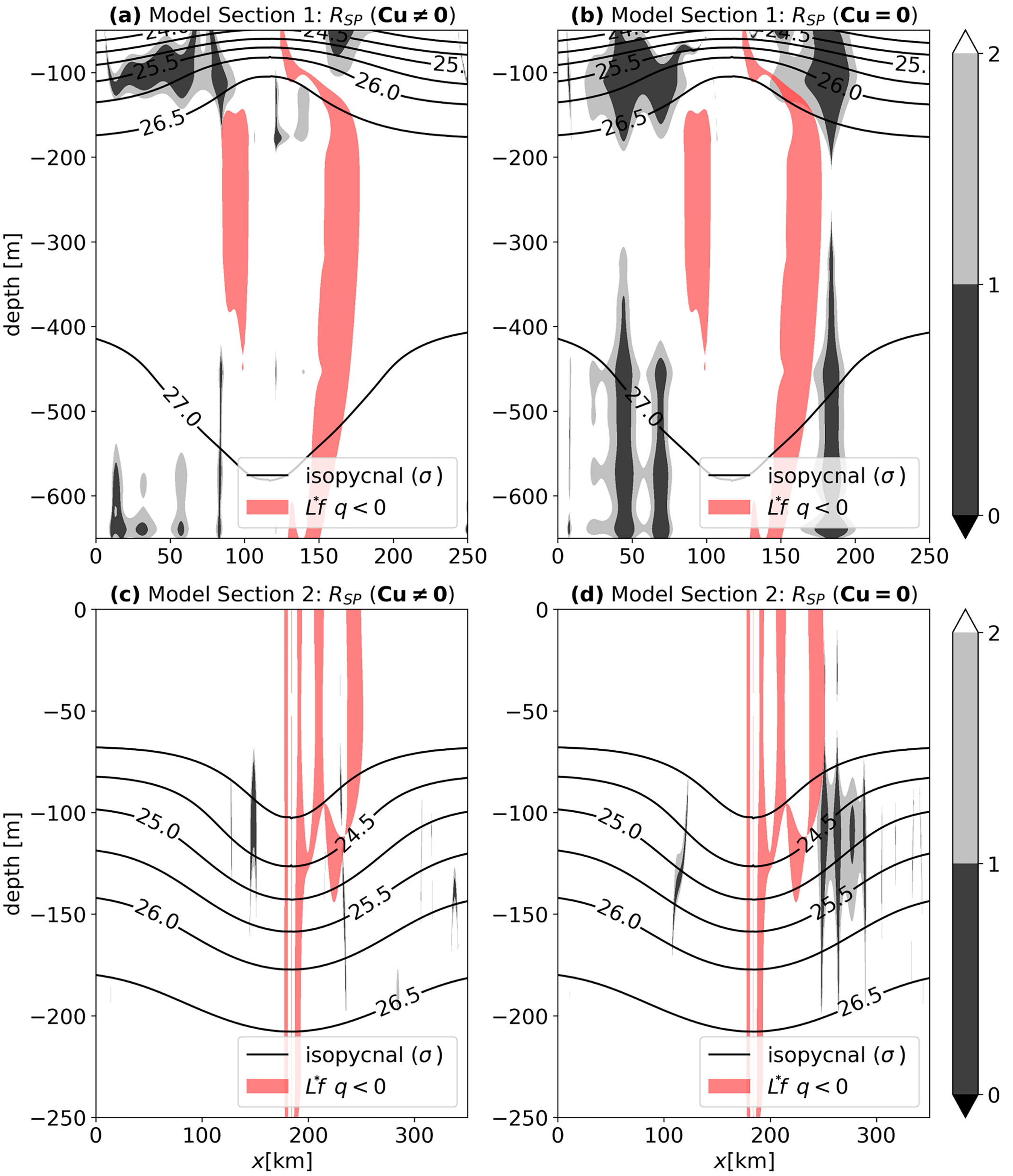

FIG. 6. The R_{SP} from the analytical model of section 1: (a) with Cu ≠ 0 and (b) with Cu = 0 and section 2: (c) with Cu ≠ 0 and (d) with Cu = 0. Regions where $L^*fq < 0$ are in red spots. Dark lines show modeled isopycnals.

disturbance, respectively, and $M^2 = \partial_r b$), we can express the linear growth rate ω of disturbances in a baroclinic vortex as

$$\omega^2 = -\frac{f^2 L^* q^*}{1 + \tau^2}. \tag{16}$$

In this expression, the nondimensional quantity L^*q^* has previously been defined [Eq. (5)]. The $\tau = k/m$ is the aspect ratio of the disturbance, and note that for $\tau \ll 1$ (i.e., large horizontal scale and small vertical scale), Eq. (16) reduces to $\omega^2 \approx -f^2L^*q^*$. In the geostrophic case ($L^* = 1$), a thermal wind balance can be assumed, and we recover published growth rates for symmetric instability within a geostrophic front: $\omega^2 = -f^2q^* = -f(f + \zeta) + M^4/N^2$ (Ooyama 1966; Thomas et al. 2013). In the work that follows, we denote the characteristic time scale of the disturbance as $T_c = \omega^{-1}$. This can be easily computed for a two-dimensional vertical section.

Figure 7 depicts the characteristic time scale of development of the instability (in days) for both the data and the analytical model with and without curvature. Overall, the characteristic time scale is larger when including the local curvature of the flow. Mathematically, this can be explained using the fact that, for an anticyclonic eddy in the Northern

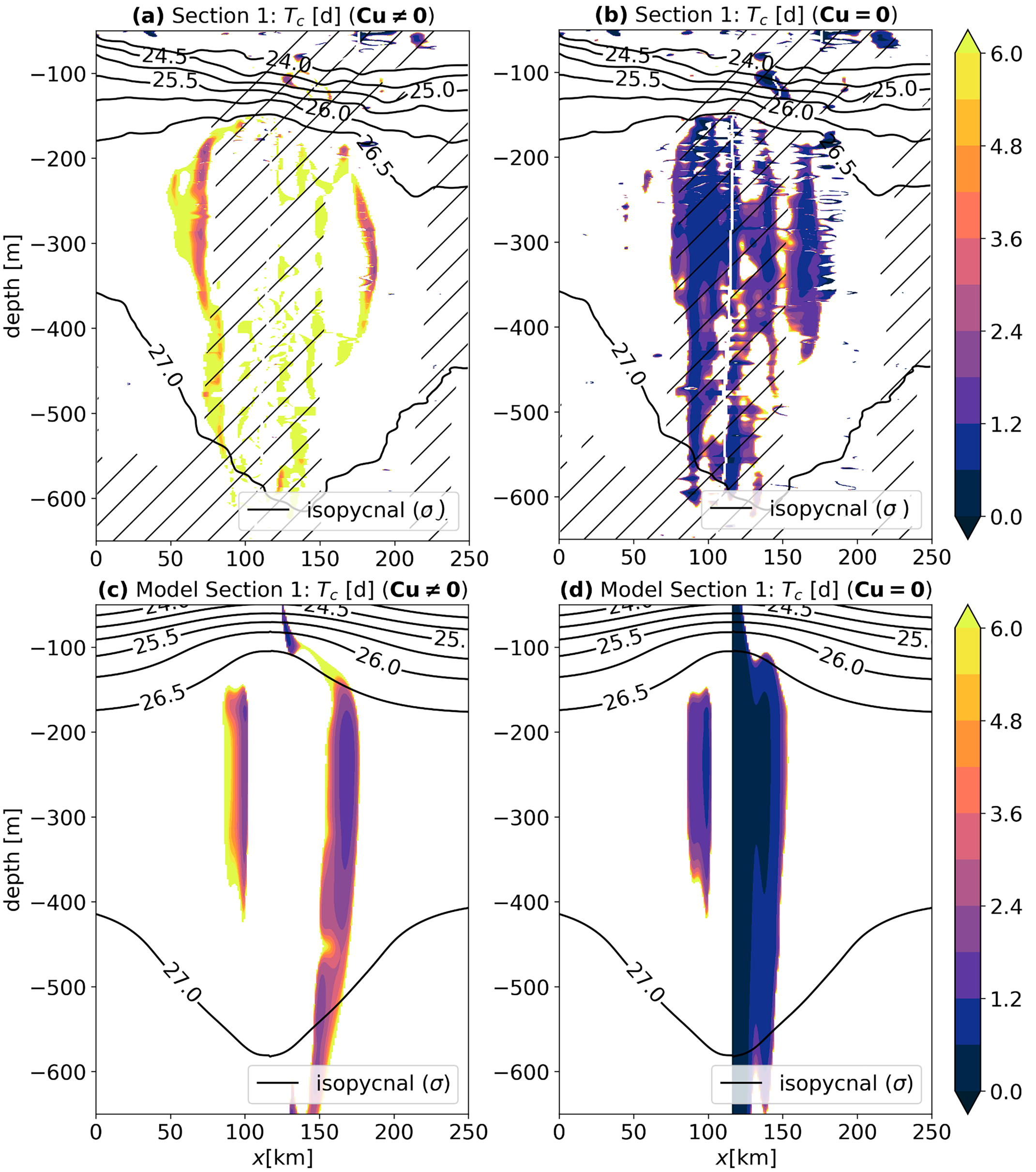

FIG. 7. Characteristic time of CSI development in days using (a),(b) the observations and (c),(d) the analytical model and when (a),(c) considering and (b),(d) neglecting the curvature. Dark lines are isopycnal surfaces.

Hemisphere and neglecting the baroclinic aspect of the flow, we have $1 + \mathrm{Cu} < 1$, giving a ω smaller than would otherwise be the case. This is particularly evident in time scales estimated from the analytical representations of the data (Figs. 7c and d). For those panels depicting values estimated from the data, i.e., Figs. 7a and b, this is less obvious; regions subject to CSI are also highly dependent on the local curvature and are thus not the same across panels. Nevertheless, we observe a qualitative trend of longer time scales (warmer colors) when considering curvature [(Fig. 7a) than when neglecting curvature (Fig. 7b). According to the model accounting for curvature, the fastest growing mode of CSI has a time scale shorter than 1.5 days. This is consistent with a previous finding on the subject, obtained using a different method (Goldsworth 2022).

A comparison with the rotating period of fluid particles at the radius of maximum velocity can be made. Assuming an axisymmetric, subsurface anticyclonic eddy with a 75-km radius and an azimuthal velocity on the order of 1 m s^{-1}, a fluid particle completes a full revolution of the eddy perimeter in approximately 5 days and a half, which is 3.3 times higher than the characteristic time of CSI development. This comparison is made to show that the changes in the structure of the vortex due to the symmetrical instability will be perceptible in a very short time and not in a time characteristic of the vortex (its period of rotation) or in a very long time (where other phenomena could mask them). Here, turbulence is not taken into account, and we know that it can increase the instability time scale by a factor of 4 (Goldsworth 2022).

We can also confront this fastest growing mode with the inertial period defined as $2\pi/f \approx 2.8$ days in this region, which is 1.9 times higher than the characteristic time of CSI development.

Concerning the sampling time periods of sections—which goes from 1 day 14 h 40 min for section 1 to 2 days 13 h 30 min for section 2—we observe that it is of the same order than the fastest growing mode of CSI but not much smaller. As it is the case for most studies based on observations, we only consider an average state of eddies with different profiles collected at different times.

7. Conclusions

In this article, two conditions for CSI are applied on two anticyclonic eddies sampled by ships during EUREC4A-OA experiment. One appears as a surface NBC ring, whereas the other possesses a deeper, intrathermocline structure. This is probably one of the first observational-based works to address the hypothesis that symmetric instability is active in North Brazil Current rings. Our results suggest that mesoscale eddies could be subject to the centrifugal–symmetric instability (CSI) even if they lie below the pycnocline. That is, their dynamics can be unstable due to their lateral or vertical shear and the curvature of the flow. Regions subject to CSI are located close to the inflection point of isopycnals, implying an extremum in the radial gradient of buoyancy which is also close to regions where the vertical shear is greatest.

Finally, we gave arguments toward possible CSI occurring in mesoscale eddies which do not lie at the surface. CSI seems to occur close to the radius of maximum velocity relatively quickly as the characteristic time of development for inviscid linear symmetric modes is smaller than 1.5 days, which is consistent with previous numerical studies in the region. In reality, turbulent viscosity may erode the smallest and fastest growing instability modes leading to remaining modes with longer time scales. Future studies should focus on the impact of such instabilities on the mixing of water masses. Indeed, this mixing may change the heat and salt content of such structures, as well as their life cycle, transferring kinetic energy to smaller scales.

Via this study, we showed that the curvature of the flow can have a significant influence on the energy budget of CSI development as well as on their growth rate which is reduced when accounting for the curvature effect. An important conclusion of this study is that future studies should take into account the curvature parameter Cu for CSI analyses in eddies, rather than considering only the geostrophic flow.

Acknowledgments. This research has been supported by the European Union Horizon 2020 research and innovation program under Grant Agreements 817578 (TRIATLAS), 101118693 (ERC Synergy WHIRLS https://whirls.eu), and 101060452 (OCEAN:ICE, https://ocean-ice.eu); the Centre National d'Etudes Spatiales through the EUREC4A-OA project; the French national programme LEFE INSU; IFREMER; the French vessel research fleet; the French research infrastructures AERIS and ODATIS; IPSL; the Chaire Chanel programme of the Geosciences Department at ENS; and the EUREC4A-OA JPI Ocean and Climate programme. We would also like to extend our gratitude to the captains, crews, and scientists of the R/V *Atalante*. Yan Barabinot is supported by a Ph.D grant from Ecole Normale Supérieure de Saclay. Xavier Carton acknowledges support by UBO. Christian Buckingham is grateful for salary support from NOC, Southampton. The authors report no conflict of interest.

Data availability statement. This study made use of a number of datasets that were made available to us freely. The concatenated R/Vs *Atalante* and *Maria S. Merian* hydrographic and velocity data (L'Hégaret et al. 2023) are freely available for download from the SEANOE website at https://www.seanoe.org/data/00809/92071/, accessed on 15 March 2021.

APPENDIX A

Turbulent Kinetic Energy Sources for a Baroclinic Front in Gradient Wind Balance

Our mathematical model is based on the equations of motion for an incompressible, inviscid, nondiffusive, Boussinesq fluid on the f plane (Buckingham et al. 2021a). We assume an axisymmetric vortex flow in cyclogeostrophic and hydrostatic balance (i.e., gradient wind balance) whose velocity field is perturbed by CSI. In terms of cylindrical coordinates $\{r, \theta, z\}$ (which represent radial, azimuthal, and vertical directions, respectively), we denote steady and perturbed flows, respectively, as $\{0, V(r, z), 0\}$ and $\{u', v', w'\}$. We additionally introduce the background buoyancy B, perturbed buoyancy b', and reduced pressure perturbation $\pi' = p/\rho_0$, which is not necessarily in hydrostatic balance. Written in terms of the radial stratification, the base state is therefore $M^2 = \partial_r B = (f + 2V/r)\partial_z V$. By confining the solution to large r (e.g., $r \sim r_0$ that $mr_0 \gg 1$), we can assume a normal-mode solution of form $\phi' \sim e^{i(kr+mz-\omega t)}$ (Buckingham et al. 2021a). As previously mentioned in section 6, ω is the growth rate and k and m denote the radial and vertical wavenumbers of the disturbance, respectively.

The governing equation for the evolution of perturbation kinetic energy can be written as

$$\frac{\partial \langle K' \rangle}{\partial t} = -r\frac{\partial \Omega}{\partial r}\langle u'v' \rangle - \langle v'w' \rangle \frac{\partial V}{\partial z} + \langle w'b' \rangle - \frac{\partial}{\partial r}\langle u'\pi' \rangle - \frac{\partial}{\partial z}\langle w'\pi' \rangle, \qquad \text{(A1)}$$

where $K' = (u'^2 + v'^2 + w'^2)/2$ is referred to as the turbulent kinetic energy (TKE); we have ignored azimuthal variations in the flow, and for brevity, we denote the background angular velocity by $\Omega = V/r$ (Smyth and McWilliams 1998; Brannigan 2016). The angled brackets $\langle \cdot \rangle = \int_0^{2\pi} r\, d\theta \int_0^{2\pi/m} dz$ represent the volume average over one vertical wavelength ($m \neq 0$). We also define the background relative vorticity as $\zeta = \partial_r V + V/r$. On the right-hand side of Eq. (A1), the first term is the horizontal shear production (HSP) term, the second is the vertical shear production (VSP) term, and the third is the buoyancy flux (BF). The fourth and fifth terms denote the radial and vertical divergences of the radial and vertical energy fluxes, respectively.

To evaluate the relative amplitude of the three production terms, we search for convenient expressions for $R_{\mathrm{SP}} \triangleq \mathrm{HSP}/\mathrm{VSP}$, the ratio between shear production terms, and $R_{\mathrm{BS}} \triangleq \mathrm{BF}/\mathrm{VSP}$, the ratio between the buoyancy flux and the vertical shear production terms. Introducing the barotropic Rayleigh discriminant $\chi^2 = (f + 2\Omega)(\zeta + f)$ and aspect ratio $\tau = k/m$ and defining an angle β such that $\tan(\beta) = -\tau$, we can write

$$R_{\mathrm{SP}} = \frac{[\chi^2 - (f + 2\Omega)^2]}{\tan(\beta) M^2}, \tag{A2}$$

$$R_{\mathrm{BS}} = -\frac{M^2 - N^2\tan(\beta)}{\chi^2 - M^2\tan(\beta)}\left[\frac{(f + 2\Omega)^2}{M^2}\right]. \tag{A3}$$

Modes aligned with isopycnals ($k/m = M^2/N^2$) maximize the growth rate ω of CSI (Thomas et al. 2013; Bachman and Taylor 2014; Brannigan et al. 2017; Buckingham et al. 2021a; Kimura 2024). Ratios thus simplify as

$$R_{\mathrm{SP}} = \frac{N^2}{M^4}[\chi^2 - (f + 2\Omega)^2], \tag{A4}$$

$$R_{\mathrm{BS}} = 0. \tag{A5}$$

That R_{BS} vanishes is logical since there is minimal buoyancy flux for instabilities in which parcel motion is along isopycnals—i.e., pure SI. As before, we introduce the dynamical Rossby number $\mathrm{Ro}_d = \zeta/f$, the dynamical Richardson number $\mathrm{Ri}_d = (f + 2\Omega)^2 N^2/M^4$, and curvature number $\mathrm{Cu} = 2V/(fr) = 2\Omega/f$. For a curved front in gradient wind balance subject to CSI, the ratio between shear production terms for modes maximizing ω is then

$$R_{\mathrm{SP}} = -\frac{\mathrm{Ro}_d\,\mathrm{Ri}_d}{(1 + \mathrm{Cu})}\left(1 - \frac{\mathrm{Cu}}{\mathrm{Ro}_d}\right). \tag{A6}$$

To better understand this expression, we consider three cases. In the limit of zero curvature ($\mathrm{Cu} = 0$), we recover the result valid for geostrophic flow (Thomas et al. 2013; Chor et al. 2022). When the curvature is nonzero and equal to the dynamical Rossby number ($\mathrm{Cu} = \mathrm{Ro}_d$), the horizontal shear production vanishes. To see this, note that radially integrating the expression $\mathrm{Cu} = \mathrm{Ro}_d$, one find that this occurs when the azimuthal velocity is of the form $V = (A - f)r$, with A being nonzero constant. This is equivalent to a linearly varying velocity profile V or solid-body rotation, for which, by definition, $\partial_r\Omega$ is zero, and so the horizontal shear production term is zero. As a final case, consider the case $\mathrm{Cu} = -1$. This implies that the nondimensional absolute angular momentum is zero: $L^* = 1 + \mathrm{Cu} = 0$. This, in turn, implies $L = 0$. For a fluid parcel experiencing a curvature number of $\mathrm{Cu} = -1$ in the Northern Hemisphere, the relative angular momentum ($rV = -fr^2/2$) will be equal but opposite in sign to the planetary angular momentum ($fr^2/2$), such that fluid parcels are no longer bound but translate radially outward. In this case, the vertical shear production tends to zero and $R_{\mathrm{SP}} \to \infty$. This particular case corresponds to an extremely intense anticyclonic vortex flow. For example, for a Gaussian velocity profile $V(r)$, this requires $\mathrm{Ro}_d = -2$ at the radius of maximum velocity.

APPENDIX B

Sensitivity Study

The raw potential density and velocity fields were smoothed with a numerical fourth-order, low-pass filter (scipy.signal.filt in Python) to avoid overshoots when computing gradients. As we were considering mesoscale eddies, we choose thresholds $L_x = 20$ km and $L_z = 20$ m for the horizontal and vertical length scales. The cutoff length scales (L_x, L_z) of filters are chosen to be longer than the spatial sampling of the calibrated data. Nevertheless, this mapping could lead to artifacts when computing gradients, and we perform a sensitivity study in Fig. B1. As we can see, whatever the smoothing period values, regions where the cyclogeostrophic criterion is matched are still found at the edge of eddies.

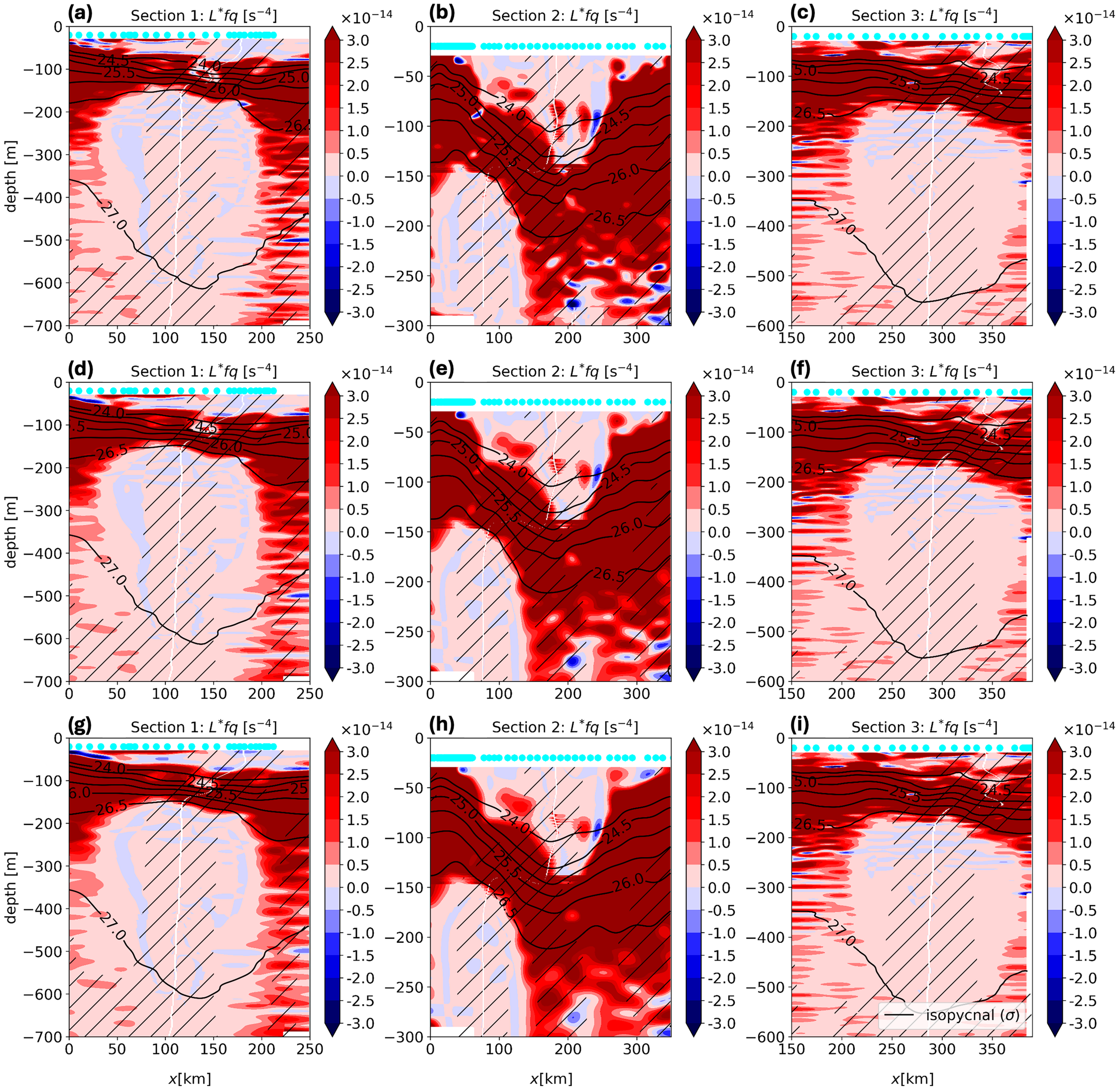

FIG. B1. The cyclogeostrophic criterion $L^*fq < 0$ (Buckingham et al. 2021a,b) for several smoothing periods. (a)–(c) L_x = 30 km and L_z = 30 m. (d)–(f) L_x = 40 km and L_z = 40 m. (g)–(i) L_x = 50 km and L_z = 50 m. Dark lines are isopycnal surfaces.

APPENDIX C

Discussion on the Axisymmetric Hypothesis

In this part, we discuss the validity of the axisymmetric approximation. As the subsurface anticyclonic eddy is not detected at the sea surface, we focus on the surface NBC rings of section 2. The aim is to build an analytical model for the streamfunction and analyze the impact of the asymmetry on the Ertel PV and absolute angular momentum or curvature.

To assess its horizontal extent, we use the TOEddies algorithm which has proved to be efficient in detecting mesoscale eddies with satellite data (Laxenaire et al. 2018, 2024; Ioannou et al. 2024). During the field experiments, this detection was applied to ad hoc near-real-time (NRT) absolute dynamic topography (ADT) maps. We used daily all-satellite sea surface height fields provided by the Copernicus Marine Service (https://marine.copernicus.eu/fr). This multisatellite product integrates data from all available satellites at any given time and projects it onto a fixed grid with a resolution of 1/4°, covering the global ocean. The products used include the CNES-CLS18 mean dynamic topography (MDT) (Mulet et al. 2021), which serves as the standard for Data Unification and Altimeter Combination System–Delayed Time 2018 (DUACS-DT2018) (Taburet et al. 2019).

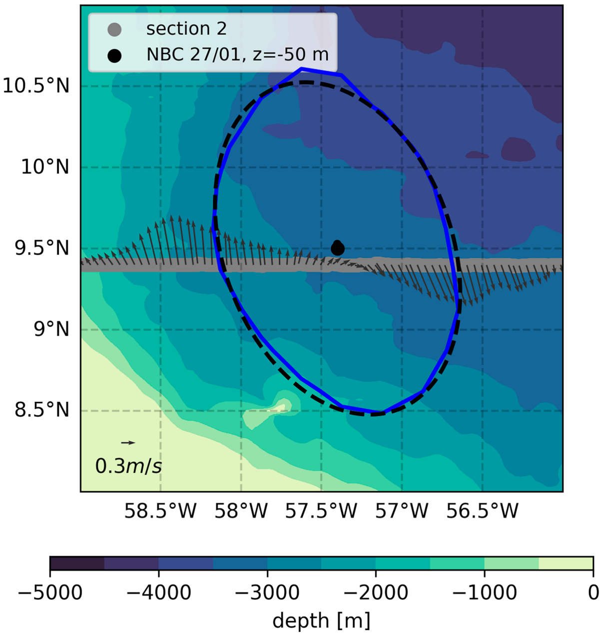

FIG. C1. Maximum velocity contour of the surface NBC ring detected using the TOEddies algorithm on 27 Jan (blue contour). Section 2 is plotted in gray, and the in situ velocity vectors are plotted in dark arrows. The elliptical model is plotted in dark dashed line. The dark dot is the eddy center, and the topography is that of Smith and Sandwell (1997).

Figure C1 shows the maximum velocity contour of the NBC rings detected by TOEddies in blue.

Considering this maximum velocity contour as an ellipsis, we propose an analytical expression to model the streamfunction of the NBC ring. For all calculations, we consider the f-plane approximation. According to Carton and McWilliams (1989) (see also Castelão and Johns 2011), the streamfunction of the surface NBC ring can be modeled as

$$\psi(r,\,\theta,\,z) = \psi_0(z)\exp\left(\frac{1}{\alpha}\left\{1 - \left[\frac{r}{R_m(\theta)}\right]^{\alpha}\right\}\right), \qquad \text{(C1)}$$

with ψ_0 being the amplitude which depends on z, α being the steepness, and R_m being the radius which depends on θ. The r is the radial coordinate from the eddy center, θ is the angle from the zonal direction, and z is the depth coordinate. Note that this formula is not, strictly speaking, that of Carton and McWilliams (1989) as we introduce the dependence in z for ψ_0 and in θ for R_m.

For an elliptic eddy, we have

$$R_m(\theta) = \frac{R_0}{\sqrt{1 - e^2\cos^2(\theta - \theta_0)}}, \qquad \text{(C2)}$$

with R_0 being the semi minor axis, e being the eccentricity, and θ_0 being the inclination of the semimajor axis with respect to the horizontal. We also define the semimajor axis R_1 so that we can compute $e = \sqrt{R_1^2 - R_0^2}/R_0$. For the NBC rings, we have $R_1 = 117$ km, $R_0 = 78$ km, $\theta_0 \approx 11\pi/18$, and $e = 0.75$. In Fig. C1, the model is plotted in dark dashed lines, and we see that it fits the maximum velocity contour very well. Note that section 2 has been performed at $\theta = 0$.

In the following, we will assume $e^2\cos^2(\theta - \theta_0)$ to be small such that we can write $R_m(\theta) \approx R_0[1 + e^2\cos^2(\theta - \theta_0)/2]$. By noting $\overline{\psi}(r, z) = \psi_0(z)\exp\{[1 - (r/R_0)^\alpha]/\alpha\}$, the streamfunction of the circular flow of radius R_0, the ellipticity adds a perturbation such that

$$\psi(r,\,\theta,\,z) = \overline{\psi}(r,\,z)\left[1 + \varepsilon(\theta)\left(\frac{r}{R_0}\right)^{\alpha}\right], \qquad \text{(C3)}$$

at order $\varepsilon(\theta)$, where $\varepsilon(\theta) = e^2\cos^2(\theta - \theta_0)/2$. Then, using $v_\theta = -\partial_r\psi$ and $v_r = \partial_\theta\psi/r$, we can compute the velocity component and obtain

$$v_\theta(r,\,\theta,\,z) = \frac{\overline{\psi}(r,\,z)}{R_0}\left(\frac{r}{R_0}\right)^{\alpha-1}\left\{1 + \left[\left(\frac{r}{R_0}\right)^{\alpha} - \alpha\right]\varepsilon(\theta)\right\}, \qquad \text{(C4)}$$

$$v_r(r,\,\theta,\,z) = \frac{\overline{\psi}(r,\,z)}{r}\left(\frac{r}{R_0}\right)^{\alpha}\varepsilon'(\theta), \qquad \text{(C5)}$$

with $\varepsilon'(\theta)$ being the derivative of $\varepsilon(\theta)$.

a. *Curvature parameter Cu*

In the axisymmetric case, we note $\overline{\mathrm{Cu}} = 2\overline{v_\theta}/(fr)$ with $\overline{v_\theta} = \overline{\psi}(r, z)/R_0(r/R_0)^{\alpha-1}$. Thus, we have

$$\mathrm{Cu} = \overline{\mathrm{Cu}}\left\{1 + \left[\left(\frac{r}{R_0}\right)^{\alpha} - \alpha\right]\varepsilon(\theta)\right\}. \qquad \text{(C6)}$$

For section 2 ($\theta = 0$), considering the eddy edge ($r \approx R_0$) with $\alpha = 2$, we obtain $\mathrm{Cu} \approx 0.97\overline{\mathrm{Cu}}$. The axisymmetric hypothesis is justified for the curvature parameter.

b. *Horizontal component of Ertel PV, q_h*

Under thermal wind balance, the horizontal component of Ertel PV q_h can be written such that

$$q_h = -f[(\partial_z v_r)^2 + (\partial_z v_\theta)^2]. \qquad \text{(C7)}$$

Compared to the axisymmetric case, we have an extra term in the expression of q_h. With some algebra, we can prove that

$$\frac{(\partial_z v_\theta)^2}{(\partial_z v_r)^2} = \frac{\left\{1 + \left[\left(\frac{r}{R_0}\right)^{\alpha} - \alpha\right]\varepsilon(\theta)\right\}^2}{[\varepsilon'(\theta)]^2}. \qquad \text{(C8)}$$

For section 2 ($\theta = 0$), considering the eddy edge ($r \approx R_0$) with $\alpha = 2$, we obtain $(\partial_z v_\theta)^2 \approx 29(\partial_z v_r)^2$. Therefore, the axisymmetry is justified for the horizontal component of Ertel PV in the case of section 2. We even underestimate a little this quantity when considering the eddy axisymmetric.

c. *Vertical component of Ertel PV, q_z*

The vertical component of Ertel PV is expressed as

$$q_z = (\partial_r v_\theta + v_\theta/r - \partial_\theta v_r/r + f)\partial_z b. \qquad \text{(C9)}$$

We define $\zeta = \partial_r v_\theta + v_\theta/r - \partial_\theta v_r/r$. Noting $\overline{\zeta}$ being the axisymmetric relative vorticity, it can be proved that

$$\zeta = \overline{\zeta}\left\{1 + \left[\left(\frac{r}{R_0}\right)^\alpha - \alpha\right]\varepsilon(\theta)\right\} - \frac{\overline{\psi}(r, z)}{r^2}\left(\frac{r}{R_0}\right)^\alpha \varepsilon''(\theta), \qquad \text{(C10)}$$

with $\varepsilon''(\theta)$ being the second derivative of $\varepsilon(\theta)$. For section 2 ($\theta = 0$), considering the eddy edge ($r \approx R_0$) with $\alpha = 2$, the first time scales as $0.97\psi_0/R_0^2$ while the second scales as $0.4\psi_0/R_0^2$. They are of the same order of magnitude and share the same sign. In the case of section 2, we therefore underestimate the relative vorticity when considering the axisymmetry approximation. Consequently, the dynamical Rossby number is smaller in absolute value in the axisymmetric approximation, and the flow is thus less likely to be unstable.

APPENDIX D

Discussion on the Resolution

The resolution has an impact on results as it drives uncertainties on the curvature parameter. In this part, we determine which error in r would be needed to stabilize the regions that have been identified as unstable (using the cyclogeostrophic criterion). We thus consider a region where $(1 + \mathrm{Cu})q < 0$. We introduce scales V for v_θ, B for b, H for z, and R_0 for r. We define $\overline{q} = q/(BV/R_0H)$, the Ertel PV without dimension, and note with an overline every quantity without dimension. As gradients have been computed using a centered scheme of order two, only errors on v_θ/r (errors of order one) will be taken into account in the analysis. Introducing the error Δr in r, the uncertainty on Cu is $\Delta\mathrm{Cu} = \mathrm{Cu}\Delta\overline{r}/\overline{r}$ and the uncertainty on $\overline{q}$ is given by $\Delta\overline{q} = (\overline{v}_\theta\overline{N}^2/\overline{r}) \times (\Delta\overline{r}/\overline{r})$. Therefore, we search for the value of $\Delta\overline{r}$ that makes $(1 + \mathrm{Cu} + \Delta\mathrm{Cu})(\overline{q} + \Delta\overline{q})$ positive when $(1 + \mathrm{Cu})\overline{q}$ is negative. By definition, every quantity denoted by an overline is of order one. Therefore, after some algebra to isolate the ratio $\Delta\overline{r}/\overline{r}$, the quantity $(1 + \mathrm{Cu} + \Delta\mathrm{Cu})(\overline{q} + \Delta\overline{q})$ is positive with $(1 + \mathrm{Cu})\overline{q}$ negative when

$$\frac{\Delta\overline{r}}{\overline{r}} > \frac{1 + \mathrm{Cu}}{1 + 2\mathrm{Cu}}. \qquad \text{(D1)}$$

In this article, regions where the cyclogeostrophic criterion (Buckingham et al. 2021a,b) is satisfied correspond to regions where $1 + \mathrm{Cu} < 0.2$. Therefore, $\Delta\overline{r}/\overline{r}$ must be higher than 0.2. For eddies with a radius larger than 80 km, we have $\Delta r > 16$ km. The resolution of our data is below this limit, but we remain at the same order of magnitude. That is why our results are not irrefutable. The analytical model proposed in part 5 is also motivated by this result.

REFERENCES

Allen, J., and P. Newberger, 1998: On symmetric instabilities in oceanic bottom boundary layers. *J. Phys. Oceanogr.*, **28**, 1131–1151, https://doi.org/10.1175/1520-0485(1998)028<1131:OSIIOB>2.0.CO;2.

Arnason, G., G. Haltiner, and M. Frawley, 1962: Higher-order geostrophic wind approximations. *Mon. Wea. Rev.*, **90**, 175–185, https://doi.org/10.1175/1520-0493(1962)090<0175:HGWA>2.0.CO;2.

Aubert, O., M. L. Bars, P. L. Gal, and P. S. Marcus, 2012: The universal aspect ratio of vortices in rotating stratified flows: Experiments and observations. *J. Fluid Mech.*, **706**, 34–45, https://doi.org/10.1017/jfm.2012.176.

Bachman, S. D., and J. R. Taylor, 2014: Modelling of partially-resolved oceanic symmetric instability. *Ocean Modell.*, **82**, 15–27, https://doi.org/10.1016/j.ocemod.2014.07.006.

Barabinot, Y., S. Speich, and X. Carton, 2024: Defining mesoscale eddies boundaries from in-situ data and a theoretical framework. *J. Geophys. Res. Oceans*, **129**, e2023JC020422, https://doi.org/10.1029/2023JC020422.

——, ——, and ——, 2025: Insights into mesoscale eddy dynamics: A three-dimensional perspective on potential density anomalies. *Ocean Sci.* , **21**, 2527–2553, https://doi.org/10.5194/os-21-2527-2025.

Beckers, M., R. Verzicco, H. Clercx, and G. J. F. Van Heijst, 2001: Dynamics of pancake-like vortices in a stratified fluid: Experiments, model and numerical simulations. *J. Fluid Mech.*, **433**, 1–27, https://doi.org/10.1017/S0022112001003482.

Bonnier, M., O. Eiff, and P. Bonneton, 2000: On the density structure of far-wake vortices in a stratified fluid. *Dyn. Atmos. Oceans*, **31**, 117–137, https://doi.org/10.1016/S0377-0265(99)00030-5.

Bowman, J. C., and T. G. Shepherd, 1995: Nonlinear symmetric stability of planetary atmospheres. *J. Fluid Mech.*, **296**, 391–407, https://doi.org/10.1017/S0022112095002175.

Brannigan, L., 2016: Intense submesoscale upwelling in anticyclonic eddies. *Geophys. Res. Lett.*, **43**, 3360–3369, https://doi.org/10.1002/2016GL067926.

——, D. P. Marshall, A. C. N. Garabato, A. G. Nurser, and J. Kaiser, 2017: Submesoscale instabilities in mesoscale eddies. *J. Phys. Oceanogr.*, **47**, 3061–3085, https://doi.org/10.1175/JPO-D-16-0178.1.

Bretherton, F. P., 1966: Critical layer instability in baroclinic flows. *Quart. J. Roy. Meteor. Soc.*, **92**, 325–334, https://doi.org/10.1002/qj.49709239302.

Buckingham, C. E., and Coauthors, 2016: Seasonality of submesoscale flows in the ocean surface boundary layer. *Geophys. Res. Lett.*, **43**, 2118–2126, https://doi.org/10.1002/2016GL068009.

——, N. S. Lucas, S. E. Belcher, T. P. Rippeth, A. L. Grant, J. Le Sommer, A. O. Ajayi, and A. C. Naveira Garabato, 2019: The contribution of surface and submesoscale processes to turbulence in the open ocean surface boundary layer. *J. Adv. Model. Earth Syst.*, **11**, 4066–4094, https://doi.org/10.1029/2019MS001801.

——, J. Gula, and X. Carton, 2021a: The role of curvature in modifying frontal instabilities. Part I: Review of theory and presentation of a nondimensional instability criterion. *J. Phys. Oceanogr.*, **51**, 299–315, https://doi.org/10.1175/JPO-D-19-0265.1.

——, ——, and ——, 2021b: The role of curvature in modifying frontal instabilities. Part II: Application of the criterion to curved density fronts at low Richardson numbers. *J. Phys. Oceanogr.*, **51**, 317–341, https://doi.org/10.1175/JPO-D-20-0258.1.

Carton, X., 2001: Hydrodynamical modeling of oceanic vortices. *Surv. Geophys.*, **22**, 179–263, https://doi.org/10.1023/A:1013779219578.

——, and J. C. McWilliams, 1989: Barotropic and baroclinic instabilities of axisymmetric vortices in a quasigeostrophic model. *Mesoscale/Synoptic Coherent Structures in Geophysical Turbulence*, Elsevier Oceanography Series, Vol. 50, Elsevier, 225–244.

Castelão, G. P., and W. E. Johns, 2011: Sea surface structure of North Brazil Current rings derived from shipboard and moored acoustic Doppler current profiler observations. *J. Geophys. Res.*, **116**, C01010, https://doi.org/10.1029/2010JC006575.

Cho, H.-R., T. G. Shepherd, and V. A. Vladimirov, 1993: Application of the direct Liapunov method to the problem of symmetric stability in the atmosphere. *J. Atmos. Sci.*, **50**, 822–836, https://doi.org/10.1175/1520-0469(1993)050<0822:AOTDLM>2.0.CO;2.

Chor, T., J. O. Wenegrat, and J. Taylor, 2022: Insights into the mixing efficiency of submesoscale centrifugal–symmetric instabilities. *J. Phys. Oceanogr.*, **52**, 2273–2287, https://doi.org/10.1175/JPO-D-21-0259.1.

D'Asaro, E., C. Lee, L. Rainville, R. Harcourt, and L. Thomas, 2011: Enhanced turbulence and energy dissipation at ocean fronts. *Science*, **332**, 318–322, https://doi.org/10.1126/science.1201515.

de Marez, C., T. Meunier, M. Morvan, P. L'hégaret, and X. Carton, 2020: Study of the stability of a large realistic cyclonic eddy. *Ocean Modell.*, **146**, 101540, https://doi.org/10.1016/j.ocemod.2019.101540.

Dewar, W., J. McWilliams, and M. Molemaker, 2015: Centrifugal instability and mixing in the California Undercurrent. *J. Phys. Oceanogr.*, **45**, 1224–1241, https://doi.org/10.1175/JPO-D-13-0269.1.

Dong, J., B. Fox-Kemper, H. Zhang, and C. Dong, 2021: The scale and activity of symmetric instability estimated from a global submesoscale-permitting ocean model. *J. Phys. Oceanogr.*, **51**, 1655–1670, https://doi.org/10.1175/JPO-D-20-0159.1.

Douglass, E., and J. Richman, 2015: Analysis of ageostrophy in strong surface eddies in the Atlantic Ocean. *J. Geophys. Res. Oceans*, **120**, 1490–1507, https://doi.org/10.1002/2014JC010350.

Eliassen, A., and E. Kleinschmidt Jr., 1957: Dynamic meteorology. *Geophysik II/Geophysics II*, Springer, 1–154.

Fjortoft, R., 1950: Application of integral theorems in deriving criteria of stability for laminar flows and for the baroclinic circular vortex. *Geophys. Publ.*, **17** (6), 1–52.

Flór, J.-B., 1994: Coherent vortex structures in stratified fluids. Ph.D. thesis, Technische Universiteit Eindhoven, 169 pp., https://doi.org/10.6100/IR417065.

Goldsworth, F. W., 2022: Symmetric instability in the Atlantic meridional overturning circulation. Ph.D. thesis, University of Oxford, 197 pp., https://ora.ox.ac.uk/objects/uuid:c96fdd34-aa34-4d04-9f2f-5d682bb53081/files/ds7526d00w.

——, D. P. Marshall, and H. L. Johnson, 2021: Symmetric instability in cross-equatorial western boundary currents. *J. Phys. Oceanogr.*, **51**, 2049–2067, https://doi.org/10.1175/JPO-D-20-0273.1.

Gula, J., M. J. Molemaker, and J. C. McWilliams, 2016a: Submesoscale dynamics of a Gulf Stream frontal eddy in the South Atlantic bight. *J. Phys. Oceanogr.*, **46**, 305–325, https://doi.org/10.1175/JPO-D-14-0258.1.

——, ——, and ——, 2016b: Topographic generation of submesoscale centrifugal instability and energy dissipation. *Nat. Commun.*, **7**, 12811, https://doi.org/10.1038/ncomms12811.

Haine, T. W., and J. Marshall, 1998: Gravitational, symmetric, and baroclinic instability of the ocean mixed layer. *J. Phys. Oceanogr.*, **28**, 634–658, https://doi.org/10.1175/1520-0485(1998)028<0634:GSABIO>2.0.CO;2.

Hamlington, P. E., L. P. V. Roekel, B. Fox-Kemper, K. Julien, and G. P. Chini, 2014: Langmuir–submesoscale interactions: Descriptive analysis of multiscale frontal spindown simulations. *J. Phys. Oceanogr.*, **44**, 2249–2272, https://doi.org/10.1175/JPO-D-13-0139.1.

Hoskins, B. J., 1974: The role of potential vorticity in symmetric stability and instability. *Quart. J. Roy. Meteor. Soc.*, **100**, 480–482, https://doi.org/10.1256/smsqj.42519.

Ioannou, A., A. Stegner, B. L. Vu, I. Taupier-Letage, and S. Speich, 2017: Dynamical evolution of intense Ierapetra eddies on a 22 year long period. *J. Geophys. Res. Oceans*, **122**, 9276–9298, https://doi.org/10.1002/2017JC013158.

——, L. Guez, R. Laxenaire, and S. Speich, 2024: Global assessment of mesoscale eddies with TOEddies: Comparison between multiple datasets and colocation with in situ measurements. *Remote Sens.*, **16**, 4336, https://doi.org/10.3390/rs16224336.

Johns, E., D. R. Watts, and H. T. Rossby, 1989: A test of geostrophy in the Gulf Stream. *J. Geophys. Res.*, **94**, 3211–3222, https://doi.org/10.1029/JC094iC03p03211.

Kimura, S., 2024: Initial and transient growth of symmetric instability. *J. Phys. Oceanogr.*, **54**, 115–129, https://doi.org/10.1175/JPO-D-23-0048.1.

Kloosterziel, R. C., 2010: Viscous symmetric stability of circular flows. *J. Fluid Mech.*, **652**, 171–193, https://doi.org/10.1017/S0022112009994149.

——, G. F. Carnevale, and P. Orlandi, 2007: Inertial instability in rotating and stratified fluids: Barotropic vortices. *J. Fluid Mech.*, **583**, 379–412, https://doi.org/10.1017/S0022112007006325.

L'Hégaret, P., and Coauthors, 2023: Ocean cross-validated observations from the R/Vs L'Atalante, Maria S. Merian and Meteor and related platforms as part of the EUREC^{4}A-OA/ATOMIC campaign. *Earth Syst. Sci. Data*, **15**, 1801–1830, https://doi.org/10.5194/essd-15-1801-2023.

Laxenaire, R., S. Speich, B. Blanke, A. Chaigneau, C. Pegliasco, and A. Stegner, 2018: Anticyclonic eddies connecting the western boundaries of Indian and Atlantic Oceans. *J. Geophys. Res. Oceans*, **123**, 7651–7677, https://doi.org/10.1029/2018JC014270.

——, ——, and A. Stegner, 2019: Evolution of the thermohaline structure of one Agulhas Ring reconstructed from satellite altimetry and Argo floats. *J. Geophys. Res. Oceans*, **124**, 8969–9003, https://doi.org/10.1029/2018JC014426.

——, L. Guez, A. Chaigneau, M. Isic, A. Ioannou, and S. Speich, 2024: TOEddies global mesoscale eddy Atlas colocated with Argo float profiles. SEANOE, accessed the 5th of November 2025, https://doi.org/10.17882/102877.

Legras, B., and D. G. Dritschel, 1993: Vortex stripping and the generation of high vorticity gradients in two-dimensional flows. *Appl. Sci. Res.*, **51**, 445–455, https://doi.org/10.1007/BF01082574.

Lévy, M., P. J. Franks, and K. S. Smith, 2018: The role of submesoscale currents in structuring marine ecosystems. *Nat. Commun.*, **9**, 4758, https://doi.org/10.1038/s41467-018-07059-3.

Mahdinia, M., P. Hassanzadeh, P. S. Marcus, and C.-H. Jiang, 2017: Stability of three-dimensional Gaussian vortices in an unbounded, rotating, vertically stratified, Boussinesq flow: Linear analysis. *J. Fluid Mech.*, **824**, 97–134, https://doi.org/10.1017/jfm.2017.303.

Mariotti, A., B. Legras, and D. G. Dritschel, 1994: Vortex stripping and the erosion of coherent structures in two-dimensional flows. *Phys. Fluids*, **6**, 3954–3962, https://doi.org/10.1063/1.868385.

Marshall, D. P., R. G. Williams, and M.-M. Lee, 1999: The relation between eddy-induced transport and isopycnic gradients of potential vorticity. *J. Phys. Oceanogr.*, **29**, 1571–1578, https://doi.org/10.1175/1520-0485(1999)029<1571:TRBEIT>2.0.CO;2.

——, J. R. Maddison, and P. Berloff, 2012: A framework for parameterizing eddy potential vorticity fluxes. *J. Phys. Oceanogr.*, **42**, 539–557, https://doi.org/10.1175/JPO-D-11-048.1.

McWilliams, J. C., 2016: Submesoscale currents in the ocean. *Proc. Roy. Soc.*, **472A**, 20160117, https://doi.org/10.1098/rspa.2016.0117.

Molemaker, M. J., J. C. McWilliams, and W. K. Dewar, 2015: Submesoscale instability and generation of mesoscale anticyclones near a separation of the California undercurrent. *J. Phys. Oceanogr.*, **45**, 613–629, https://doi.org/10.1175/JPO-D-13-0225.1.

Mulet, S., and Coauthors, 2021: The new CNES-CLS18 global mean dynamic topography. *Ocean Sci.*, **17**, 789–808, https://doi.org/10.5194/os-17-789-2021.

Müller, P., J. McWilliams, and M. Molemaker, 2005: Routes to dissipation in the ocean: The 2D/3D turbulence conundrum. *Marine Turbulence: Theories, Observations and Models*, Cambridge University Press, 397–405.

Napolitano, D. C., X. Carton, and J. Gula, 2024: Vertical interaction between NBC rings and its implications for South Atlantic water export. *J. Geophys. Res. Oceans*, **129**, e2023JC020741, https://doi.org/10.1029/2023JC020741.

Naveira Garabato, A. C., and Coauthors, 2019: Rapid mixing and exchange of deep-ocean waters in an abyssal boundary current. *Proc. Natl. Acad. Sci. USA*, **116**, 13 233–13 238, https://doi.org/10.1073/pnas.1904087116.

Negretti, M. E., and P. Billant, 2013: Stability of a Gaussian pancake vortex in a stratified fluid. *J. Fluid Mech.*, **718**, 457–480, https://doi.org/10.1017/jfm.2012.624.

Nencioli, F., V. S. Kuwahara, T. D. Dickey, Y. M. Rii, and R. R. Bidigare, 2008: Physical dynamics and biological implications of a mesoscale eddy in the lee of Hawai'i: Cyclone *Opal* observations during E-Flux III. *Deep-Sea Res. II*, **55**, 1252–1274, https://doi.org/10.1016/j.dsr2.2008.02.003.

Ooyama, K., 1966: On the stability of the baroclinic circular vortex: A sufficient criterion for instability. *J. Atmos. Sci.*, **23**, 43–53, https://doi.org/10.1175/1520-0469(1966)023<0043:OTSOTB>2.0.CO;2.

Oseen, C., 1912: Uber die Wirbelbewegung in einer reibenden Flussigkeit. *Ark. Mat. Astron. Fys.*, **7**, 14–26.

Penven, P., I. Halo, S. Pous, and L. Marié, 2014: Cyclogeostrophic balance in the Mozambique Channel. *J. Geophys. Res. Oceans*, **119**, 1054–1067, https://doi.org/10.1002/2013JC009528.

Rayleigh, L., 1917: On the dynamics of revolving fluids. *Proc. Roy. Soc. London*, **93**, 148–154, https://doi.org/10.1098/rspa.1917.0010.

Savelyev, I., and Coauthors, 2018: Aerial observations of symmetric instability at the North Wall of the Gulf Stream. *Geophys. Res. Lett.*, **45**, 236–244, https://doi.org/10.1002/2017GL075735.

Smith, W. H. F., and D. T. Sandwell, 1997: Global sea floor topography from satellite altimetry and ship depth soundings. *Science*, **277**, 1956–1962, https://doi.org/10.1126/science.277.5334.1956.

Smyth, W., and J. McWilliams, 1998: Instability of an axisymmetric vortex in a stably stratified, rotating environment. *Theor. Comput. Fluid Dyn.*, **11**, 305–322, https://doi.org/10.1007/s001620050095.

Solberg, H., 1936: Le mouvement d'inertie de l'atmosphere stable et son role dans la theorie des cyclones. *Sixth Assembly*, Paul Dupont, Edinburgh, Union Geodesique et Geophysique Internationale, 66–82.

Speich, S., and The Embarked Science Team, 2021: EUREC4A-OA. Cruise Report, 19 January–19 February 2020. Vessel: L'ATALANTE. Rep., 192 pp., https://doi.org/10.13155/80129.

Stevens, B., and Coauthors, 2021: EUREC^{4}A. *Earth Syst. Sci. Data*, **13**, 4067–4119, https://doi.org/10.5194/essd-13-4067-2021.

Subirade, C., P. L'Hégaret, S. Speich, R. Laxenaire, J. Karstensen, and X. Carton, 2023: Combining an eddy detection algorithm with in-situ measurements to study North Brazil Current rings. *Remote Sens.*, **15**, 1897, https://doi.org/10.3390/rs15071897.

Taburet, G., A. Sanchez-Roman, M. Ballarotta, M.-I. Pujol, J.-F. Legeais, F. Fournier, Y. Faugere, and G. Dibarboure, 2019: DUACS DT2018: 25 years of reprocessed sea level altimetry products. *Ocean Sci.*, **15**, 1207–1224, https://doi.org/10.5194/os-15-1207-2019.

Taylor, J. R., and R. Ferrari, 2010: Buoyancy and wind-driven convection at mixed layer density fronts. *J. Phys. Oceanogr.*, **40**, 1222–1242, https://doi.org/10.1175/2010JPO4365.1.

Thomas, L. N., and J. R. Taylor, 2010: Reduction of the usable wind-work on the general circulation by forced symmetric instability. *Geophys. Res. Lett.*, **37**, 103–113, https://doi.org/10.1029/2010GL044680.

——, ——, R. Ferrari, and T. M. Joyce, 2013: Symmetric instability in the Gulf Stream. *Deep-Sea Res. II*, **91**, 96–110, https://doi.org/10.1016/j.dsr2.2013.02.025.

——, ——, E. A. D'Asaro, C. M. Lee, J. M. Klymak, and A. Shcherbina, 2016: Symmetric instability, inertial oscillations, and turbulence at the Gulf Stream front. *J. Phys. Oceanogr.*, **46**, 197–217, https://doi.org/10.1175/JPO-D-15-0008.1.

van Mieghem, J. M., 1951: Hydrodynamic instability. *Compendium of Meteorology*, Amer. Meteor. Soc., 434–453, https://doi.org/10.1007/978-1-940033-70-9_37.

Wenegrat, J. O., and L. N. Thomas, 2020: Centrifugal and symmetric instability during Ekman adjustment of the bottom boundary layer. *J. Phys. Oceanogr.*, **50**, 1793–1812, https://doi.org/10.1175/JPO-D-20-0027.1.

——, J. Callies, and L. N. Thomas, 2018: Submesoscale baroclinic instability in the bottom boundary layer. *J. Phys. Oceanogr.*, **48**, 2571–2592, https://doi.org/10.1175/JPO-D-17-0264.1.

Yu, X., A. C. Naveira Garabato, A. P. Martin, D. G. Evans, and Z. Su, 2019: Wind-forced symmetric instability at a transient mid-ocean front. *Geophys. Res. Lett.*, **46**, 11 281–11 291, https://doi.org/10.1029/2019GL084309.

Zhou, H., W. Dewar, W. Yang, H. Liu, X. Chen, R. Li, C. Liu, and G. Gopalakrishnan, 2022: Observations and modeling of symmetric instability in the ocean interior in the Northwestern Equatorial Pacific. *Commun. Earth Environ.*, **3**, 28, https://doi.org/10.1038/s43247-022-00362-4.